WETTABILITY OF OXIDE THIN FILMS PREPARED BY PULSED LASER DEPOSITION: NEW INSIGHTS

SAURAV PRAKASH

(Bachelor of Technology, IIT Roorkee, India)

A THESIS SUBMITTED

FOR THE DEGREE OF **MASTER OF ENGINEERING**

DEPARTMENT OF MATERIAL SCIENCE AND ENGINEERING

NATIONAL UNIVERSITY OF SINGAPORE

2015

DECLARATION

I hereby declare that the thesis is my original work and it has been written by me in its entirety. I have duly acknowledged all the sources of information which have been used in the thesis.

This thesis has also not been submitted for any degree in any university previously.

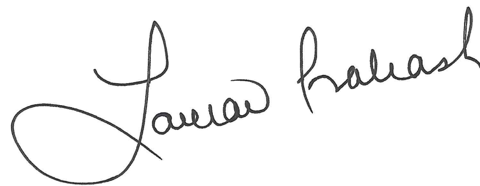

Saurav Prakash
July 31, 2015

ACKNOWLEDGEMENT

The past two years as a master's student have been instrumental in increasing my conviction towards a career in research. A lot of people have contributed towards the successful completion of my research work and thesis. I would like to express my gratitude for their help and support.

I consider myself very fortunate to have Prof. Venky Venkatesan as my supervisor. I would like to thank him for his guidance and support all along my work as a master's student. He has been very patient with me. He made sure that I had nothing else to worry about other than my research. I thank him for the defining discussions and meetings we had about the project. His mannerism, attitude and motivation towards research, insight, knowledge and speech has had a profound impact on me. He is an inspiration.

I would also like to thank Abhijeet Patra, who is like my elder brother and has worked closely with me throughout this project. I have learnt most of the experimental techniques used in the project from him. I have always turned to him for his advice about research, life, people, travel etc.. His critical inputs and complementary skills have helped me finish the project and thesis successfully.

I would like to thank Dr. Siddhartha Ghosh and Dr. Meenakshi Annamalai, who have been a part of this project, for their help and support. I would also like to thank

Dr. Surajit Saha, Dr. Sinu Matthew, Dr. Yang Ping, Dr. Natalie Mueller, Dr. Lily Mandal, Dr. Huang Zhen and Dr. Mallikarjun Motapothula for their valuable inputs and help. I would also like to thank some of the most wonderful young, talented, hardworking and helpful lab mates Han Kun, Jia Zhunan, Lim Zhi Shiuh, Michal Dykas, Soumya Sarkar, Sreetosh Goswami, Tarapada Sarkar and Zhou Wenxiong.

I would also like to thank Nanocore NUSNNI staff who have kept the lab running smoothly throughout the period of my research. I want to thank Teo Ngee Hong, Marlini Hassim, Syed Abdulrahim Syed Nizar, Sopphia Loo, Pang Bee Fong Christina and all the other people at the NUSNNI office.

I would like to thank my friends out of lab Rahul Mehta, Kartikeya Joshi, Shiva and Kumar Utkarsh for being my family away from home. Last but not the least, I would like to thank my family for their unconditional love, care and support that kept me going.

Thank you all for being there.

TABLE OF CONTENTS

Acknowledgement ... ii

Summary ... vi

List of Tables ... viii

List of Figures ... ix

List of Abbreviations ... xii

Chapter 1 ... 1

Introduction ... 1

1.1 Theory ... 2

1.1.1 Surface Tension ... 2

1.1.2 Water Contact Angle (WCA) ... 3

1.1.3 Effect of Chemical Nature on WCA ... 4

1.1.4 Effect of Roughness on WCA ... 5

1.2 Wetting studies done on Titanium Dioxide ... 6

1.3 Hydrophobicity of Rare Earth oxides (REOs) ... 7

Chapter 2 ... 13

Methods ... 13

2.1 Thin Film Fabrication (Pulsed Laser Deposition) ... 13

2.1.1 Target Preparation ... 15

2.1.2 Substrate Cleaning ... 16

2.1.3 Deposition Conditions ... 16

2.1.4 High-Pressure Reflective High Energy Electron Diffraction (RHEED) ... 17

2.2 Characterization Techniques ... 20

2.2.1 X-Ray Diffraction (XRD) ... 20

2.2.2 Atomic Force Microscopy (AFM) ... 24

2.2.3 X-Ray Photoelectron spectroscopy (XPS) ... 28

2.3 Water Contact Angle (WCA) measurement ... 30

Chapter 3 ... 33

Film Fabrication and Characterization ... 33

3.1 Pulsed laser Deposition (PLD) ... 33

3.2 Reflective High Energy Electron Diffraction (RHEED) ... 33

3.3 X-Ray Reflectometry (XRR) 34
3.4 X-ray diffraction (XRD) 36
3.5 Atomic Force Microscopy (AFM) 38
3.6 Conclusion 39
Chapter 4 40
Water Contact Angle (WCA) 40
4.1 REO series 40
4.2 Temporal study of WCA of oxide thin films 41
4.3 Conclusion 52
Appendix 56
A1 56
A1.1 Pulsed Laser Deposition (PLD) 56
A1.2 Thickness of films 56
A1.3 X-Ray Diffraction (XRD) 57
A1.4 Atomic Force Microscopy (AFM) 61
A2 62
A2.1 Pulsed Laser Deposition (PLD) 62
A2.2 Reflective High Energy Electron Diffraction (RHEED) and X-ray Reflectometry (XRR) 63
A2.3 X-ray Diffraction (XRD) 64
A2.4 Atomic Force Microscope 67
References 68

SUMMARY

The objective of the thesis is to investigate the wettability of good quality oxide thin films prepared by pulsed laser deposition (PLD). In this work, many shortfalls in the water contact angle measurement of thin films of oxides, responsible for the wide scatter in the values reported in literature, have been addressed.

Thin films of oxides of rare earth elements were made on YSZ substrates by PLD and the water contact angle (WCA) for the films was measured after environmental stabilization for about 6 weeks. Most of the films had WCA slightly below the hydrophobic mark (90˚) and a few were found to be hydrophobic.

Temporal measurements of WCA was done on epitaxial single crystal Lu_2O_3, Er_2O_3 and TiO_2 films stored in different conditions to investigate the role of environmental stabilization on wettability of the oxide film surfaces. It was found that all the oxide films in the study are intrinsically hydrophilic with a very low WCA in the range 10-20˚ when measured fresh from PLD vacuum chamber. XPS measurements suggest that the films on exposure to atmosphere get hydrated and surface adsorbs hydrocarbons (mostly alkanes) which causes the WCA to increase with time. WCA for Lu_2O_3 and Er_2O_3 films continued to increase after 6 weeks while for TiO_2 film stabilizes around ~65˚.

In a different experiment, Lu_2O_3 and Er_2O_3 films of different thickness were prepared. The ~2 u.c. film was invariably found to have a lower intrinsic WCA for both the oxides. But after saturation on exposure to the ambient atmosphere they

all were found to have nearly the same saturation value. This suggests that there is some thickness dependence or some influence of the substrate underneath which is responsible for the lower intrinsic WCA value in case of ~2 u.c. films.

LIST OF TABLES

Table 1.2.1 TiO_2 films WCA reported values in literature. 7

Table 3.1.1 PLD growth parameters 33

Table 4.3.1 Environmentally saturated WCA for REO film series...................... 53

Table 4.3.2 Intrinsic WCA for oxide films. 53

Table A1. 1 PLD growth parameters for REO films... 56

Table A1. 2 Thickness of different REO films**.** 57

Table A1. 3 Crystal Structure and Lattice parameter for REOs (Source: Crystallography Open Database) 57

Table A2. 1 PLD growth parameters for Er_2O_3. 62

Table A2. 2 PLD growth parameters for TiO_2**.**.. 62

LIST OF FIGURES

Figure 1.1.1 Schematic explaining the origin of surface tension in liquids.[6] 2

Figure 1.1.2 Young's equation. 3

Figure 1.1.3 Effect of roughness (apparent contact angle θ')[15]. 6

Figure 1.3.1 Schematic of the orientation of water molecules and associated WCA of the surface (a) Hydrophilic Alumina surface (b) Hydrophobic REO surface[21]. 8

Figure 1.3.2 Orientation of water molecule on the surface of (a) high-electronegativity metal oxide (b) low electronegativity metal oxide (c) low electronegativity metal nitride. [29] 9

Figure 1.3.3 (a)Surface atomic percent of carbon as a function of time (b) Advancing WCA as a function of time[30] 10

Figure 2.1.1 Schematic of PLD with RHEED 15

Figure 2.1.2 Neocera PLD setup 15

Figure 2.1.3 Schematic view of the RHEED geometry .Θ_I (Θ_F) and ϕ_I (ϕ_F) are the incident and azimuthal angles of incident(diffracted) beam. Rs is the distance between substrate and the phosphor screen and S the distance between the diffraction spot or streaks[46]. 17

Figure 2.1.4 Film growth modes **(a)** Layer-by-layer, **(b)** Island growth, **(c)** mixed mode and **(d)** step flow[47] 19

Figure 2.1.5 RHEED oscillations observed in layer-by-layer growth mode (Courtesy : http://www.material.tohoku.ac.jp/) 20

Figure 2.2.1 Schematic of a XRD setup 22

Figure 2.2.2 XRD setup Bruker D8 Discover 23

Figure 2.2.3 Typical XRR spectrum showing meaning of parameters. 24

Figure 2.2.4 Lennard-Jones Potential Curve... 25

Figure 2.2.5 Schematic AFM operation in tapping mode. 27

Figure 2.2.6 AFM setup. 28

Figure 2.2.7 Photoemission Process for XPS analysis....................................... 29

Figure 2.2.8 XPS instrument. 30

Figure 2.3.1 Schematic for contact angle θ 31

Figure 2.3.2 Dataphysics setup for WCA measurement. 32

Figure 3.2.1 RHEED pattern (a) YSZ substrate before deposition,(b) after 1000 laser pulses, (c) after 2000 laser pulses and (d) after 4000 pulses. (e) RHEED oscillations of the specularly reflected spot during deposition. 34

Figure 3.3.1 Reflectivity plot for lutetium oxide thin film 35

Figure 3.4.1 Schematic of Lu_2O_3 unit cell and crystal structure information…...36

Figure 3.4.2 (a) 2θ/ω plot (b) (004) rocking curve (c) (024) Phi scan of lutetium oxide film 38

Figure 3.5.1 AFM scan image (a) YSZ (001) substrate (b) Lu_2O_3 film. 38

Figure 4.1.1 WCA for REO thin films on YSZ 41

Figure 4.2.1 Average WCA for (a) Lu_2O_3 (b) Er_2O_3 films of different thickness (c) TiO_2 (~50nm) film. 43

Figure 4.2.2 1st WCA of (a) Lu_2O_3 films (b) Er_2O_3 films and (c)TiO_2 film 45

Figure 4.2.3 Droplet shape on 50 u.c. Lu2O3 film after (a)0 hr, (b)1 hr, (c)3 hr, (d)12 hr, (e)36 hr, (f)72 hr, (g)1 week, (h)2 weeks, (i)3 weeks and (j)5 weeks of exposure to ambient atmosphere. 46

Figure 4.2.4 Average WCA for (a) Lu_2O_3 (b) TiO_2 (~50nm) film after 5days storage in vacuum(1xE-7 torr) 48

Figure 4.2.5 1st WCA for Lu_2O_3 and TiO_2 film after 5 days of storage in vacuum 48

Figure 4.2.6 XPS survey spectrum of Lu_2O_3 films (a)freshly prepared(b)stored in ambient atmosphere for 3 weeks and (c)stored in vacuum for 5 days with surface composition and WCA values 50

Figure 4.2.7 High resolution (a) C1s and (b) O1s and (c) Lu 4d spectra for the three Lu_2O_3 films. 51

Figure A1. 1 2θ/ω scan for (a)Lu_2O_3 (b)Yb_2O_3 (c)Tm_2O_3 (d)Er_2O_3 (e)Ho_2O_3 (f)Dy_2O_3 (g)Eu_2O_3 (h)CeO_2 films on YSZ(001).. 60

Figure A1. 2 AFM scan images for REO films with rms roughness. 61

Figure A2. 1 RHEED pattern (a) YSZ substrate before deposition,(b) after 1000 laser pulses, (c) after 4000 laser pulses for erbium oxide film. (d) RHEED oscillations of the specularly reflected (00) spot during deposition. 63

Figure A2. 2 (a) 2θ/ω plot (b) rocking curve about (004) of Er_2O_3 film............. 65

Figure A2. 3 (a) 2θ/ω plot of titanium dioxide film on STO (001) (b) rocking curve about (004) peak of TiO_2 (c) phi scan TiO_2 {015}. 66

Figure A2. 4 AFM images with rms roughness values for (a) YSZ (001) substrate, (b) Er_2O_3 film, (c) STO (001) substrate and (d) TiO_2 film. 67

LIST OF ABBREVIATIONS

CA	Contact Angle
WCA	Water Contact Angle
PLD	Pulsed Laser Deposition
XRD	X-ray Diffraction
XRR	X-Ray Reflectometry
XPS	X-ray Photoelectron Spectroscopy
AFM	Atomic Force Microscopy
REO	Rare Earth Oxide
RHEED	Reflective High Energy Electron Diffraction
STO	Strontium Titanate($SrTiO_3$)
YSZ	Yttria-stabalized Zirconia
FTIR	Fourier Transform Infrared Spectroscopy
GATR	Grazing-angle Attenuated Total Reflection
u.c.	Unit cell

CHAPTER 1

INTRODUCTION

Wettability of a solid surface is the ability of a liquid to spread on the solid surface due to physical interactions between the two at the interface. The wetting of the surface by the liquid is related to physical chemistry (wettability), statistical physics (pinning of the contact line, wetting transitions, etc.), long-range forces (van der Waals, double layers), and fluid dynamics [1]. The study of wetting has been fueled by the need to better understand wetting dependent processes in daily life, biology and industry - adhesion, painting, cleaning, printing, lubrication, oil recovery, spray quenching, to name a few.

Wettability studies usually involve the measurement of contact angles as the primary data acquisition step, which indicates the degree of interaction between a solid and the liquid. Hence, the contact angle (CA) is a measure of the wetting property of a solid surface with reference to a chosen liquid.

Water Contact Angle (WCA), then is the quantity which is a measure of wettability of a surface with water. Water is a polar liquid whose interaction with most surfaces is of great significance. There is an increasing interest in the development of super hydrophilic surfaces, super hydrophobic surfaces and surfaces with tunable wettability. These special surfaces would find application in self-cleaning, microfluidics, droplet condensation etc. [2-5].

1.1 THEORY

1.1.1 Surface Tension

The origin of surface tension in liquids is the difference in the environment of a molecule in bulk and on the surface as shown in figure 1.1.1. A molecule in the bulk is pulled in all directions by the neighbors and the net resultant force is zero. A molecule on the surface does not have neighbors in all directions and hence experiences a net inward pull. This net force causes the liquid to contract its surface area to minimize the surface free energy. This surface force that causes the liquid surface to contract and behave as a trampoline is surface tension, alternatively characterized as surface free energy. Contact angle of a liquid on a solid surface is the result of surface tension and external forces.

Figure 1.1.1 Schematic explaining the origin of surface tension in liquids.[6]

Water is a unique self-associated liquid. In bulk, it forms an ordered three dimensional (3D) network of water molecules by hydrogen bonding. It is a polar solvent. Pure water (18.2 MΩ.cm) is known to have a surface tension value of 72.8 dy/cm [7].

1.1.2 Water Contact Angle (WCA)

The shape of a drop on surface depends on the magnitude of forces pulling at the three phase contact line of the drop with the surface. The equilibrium shape of a liquid drop on a surface is governed by Young's equation as shown in figure 1.1.2[8]. The effects of gravity can be ignored as the droplet size used for WCA measurement is small and hence the drop forms a spherical cap on top of the solid surface.

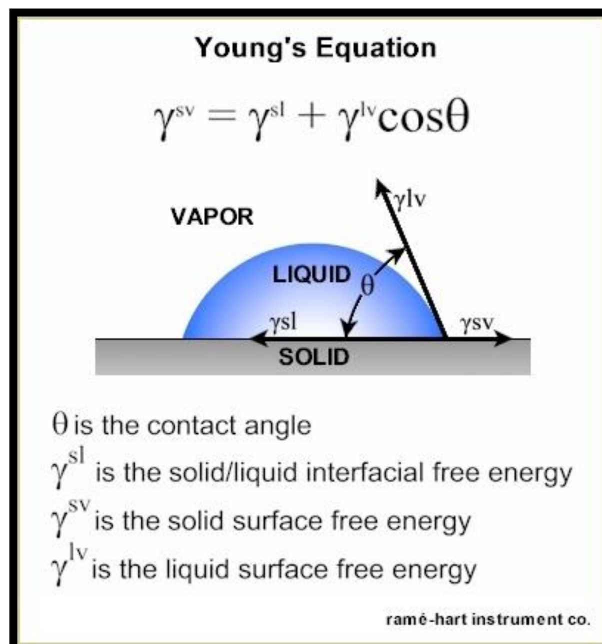

Figure 1.1.2 Young's equation.

Young's CA is a characteristic property which indicates the wettability of a surface by a liquid. It can be measured only on an ideal solid surface. An ideal solid surface is one which is smooth, chemically homogenous, insoluble, rigid and non-reactive [9].

Hydrophilic and Hydrophobic

The terms are often used in a relative sense to show the difference in interaction of water with two surfaces. But in absolute sense a surface is hydrophobic if it has a WCA greater than 90° and hydrophilic otherwise. Besides this there is separate classification for surfaces having extreme WCA. A surface having WCA greater than 150° is called as superhydrophobic or ultraphobic. For superhydrophobic surfaces there is almost no contact between the liquid drop and the surface, which can explain the "lotus effect" [13]. A surface with WCA lower than 5° is called as superhydrophilic or ultraphilic.

Surface force investigations done by Yoon et al. provided a more quantitative definition to the terms 'hydrophobic' and 'hydrophilic'[10]. The work defines WCA ≈ 65° to be the boundary about which the nature of force changes and also the structure of interfacial water changes. This limit is in close agreement with study done by Berg et al. [11].

There are two main factors that decide the Water Contact Angle on a solid surface: Chemical constituent of the surface and its roughness.

1.1.3 Effect of Chemical Nature on WCA

The chemistry of the surface decides the surface energy of the solid surface. An important property that decides the affinity of a solid surface for water is surface polarity. Generally a higher surface polarity leads to increased hydrophilicity. Surface of oxides essentially contains coordinatively unsaturated oxide anions and metal cations due to which an oxide ceramic surface is polar. The oxide ions and metal cations present on the surface act as Lewis base and acid respectively which

interact with water molecules. Polymeric modifiers make the surface less polar and are used to make metal surfaces hydrophobic [12].

1.1.4 Effect of Roughness on WCA

Roughness plays a very decisive role in the measured value for WCA. What we measure is, in fact, almost every time an apparent contact angle θ' which is different from the characteristic WCA. Wenzel's equation explains the effect of roughness [13]. It is evident from the Wenzel equation that a hydrophobic surface becomes progressively more hydrophobic as the roughness of the surface increases and likewise for a chemically hydrophilic surface.

Cassie-Baxter is a special case where in a special kind of surface structure renders any surface whether or not chemically hydrophobic in nature, hydrophobic [14]. This special roughness leads to air gaps trapped at the liquid-solid interface. Figure 1.1.3 shows both Wenzel and Cassie-Baxter equations with schematic.

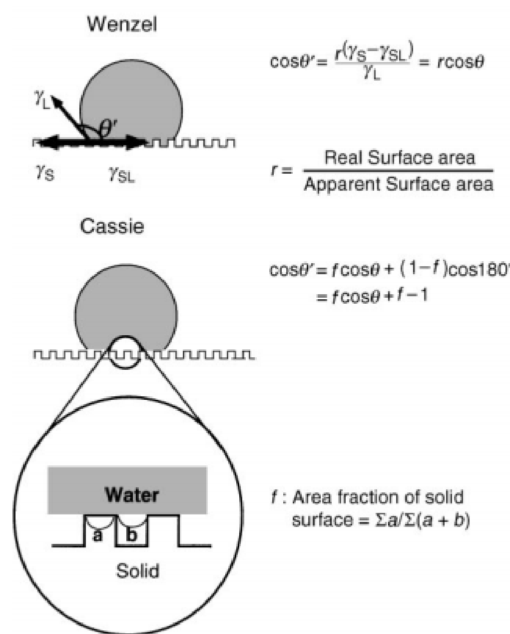

Figure 1.1.3 Effect of roughness (apparent contact angle θ')[15].

1.2 WETTING STUDIES DONE ON TITANIUM DIOXIDE

Wetting studies have been done extensively on TiO_2 thin films. The surface of TiO_2 becomes superhydrophilic (WCA ≈ 0˚) when irradiated with UV light. The reported WCA values for TiO_2 films in different studies is shown in table 1.2.1.

Table 1.2.1 TiO_2 films WCA reported values in literature.

Nature	Method	Crystallinity information	Roughness	Cleaning	WCA	
Thin Film	Dip coating	polycrystalline anatase	~1.3 nm	NA	30˚	[16]
Thin Film	Spray pyrolysis	polycrystalline anatase	NA	As prepared	54˚	[17]
				Cleaned with 4M NaOH	15˚	
Thin Film	Spray coating	polycrystalline anatase	NA	Freshly prepared	15˚	[18]
				Stored in ambient (2 months)	72˚	
Thin Film	Spin coating + annealing	NA	NA	Acetone+ DI water	50˚	[19]
Thin Film	Spin coating + annealing	polycrystalline	NA	NA	30˚	[20]

The table shows that almost all values form 15-74˚ have been reported for TiO_2 films. It is clear that in literature, only apparent values, which are not intrinsic to TiO_2 have been reported. Due to the large scatter in reported values for ZnO (not shown here), we suspect, the same applies to that system as well.

1.3 Hydrophobicity of Rare Earth oxides (REOs)

Kripa K. Varnasi et al. first reported the hydrophobic nature of the entire Rare Earth Oxide ceramics from ceria to lutecia [21]. They proposed that since the 4f cations (mostly trivalent) have a unique electronic configuration, the unfilled 4f orbitals are not allowed to interact with environment (water) by the full octet of electrons

($5s^2p^6$) [22, 23]. Consequently, the surface is less polar due to the inertness of the cations and a droplet of water beads up on the surface. Using the van Oss-Good-Chaudhary approach, they showed that indeed the polar component of surface energy of these oxide surfaces was found to be negligible. The difference in orientation of water molecule next to hydrophilic Alumina surface and hydrophobic REO surface is shown schematically in figure 1.3.1 [24-26].

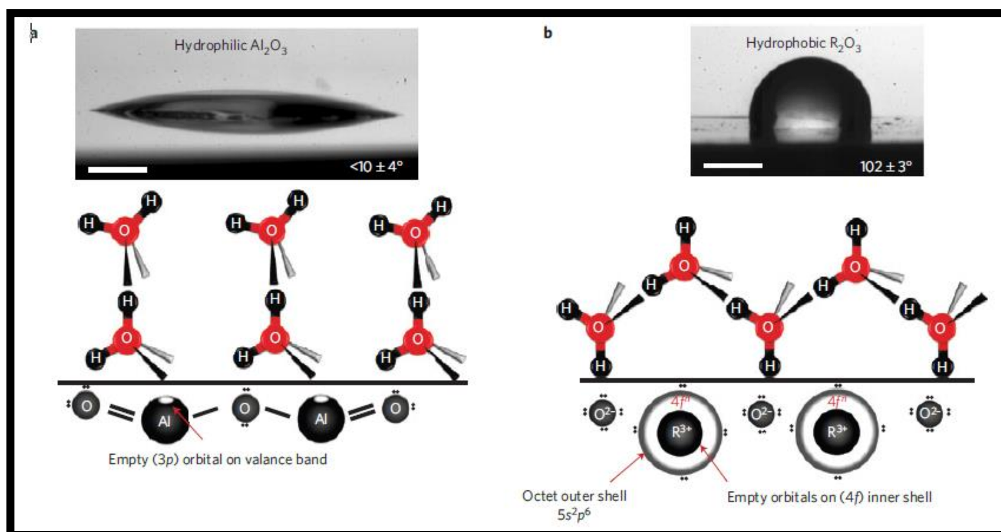

Figure 1.3.1 Schematic of the orientation of water molecules and associated WCA of the surface (a) Hydrophilic Alumina surface (b) Hydrophobic REO surface[21].

The orientation of water molecule near the interface proposed for alumina and REOs was supported by FTIR/GATR spectra [27, 28]. However, these studies were done on bulk polycrystalline ceramic pellets of REOs prepared by sintering of pressed pellets. The ceramic pellets have inherent chemical heterogeneity (polycrystalline, grain boundaries and pores) and surface roughness. Also, the role of atmospheric contamination was not discussed. With all these shortfalls it is very difficult to measure intrinsic WCA which is a material property.

Sergei Zenkin et al. showed the hydrophobic nature of various low electronegativity metals (including rare earth metal) oxides and nitrides thin films on Si(111) [29]. The work showed that a lower value of electronegativity of metal cations in case of REOs films make them hydrophobic in nature. The group also showed that nitrides of rare earth elements are more hydrophobic because nitride anions are poorer Lewis base than oxide anions. The interaction of water near the surface of the oxide and nitride sample is shown schematically in figure 1.3.2. Storage condition for samples and atmospheric contamination has not been discussed in the study. The crystallinity and roughness information is not available for the films in the study.

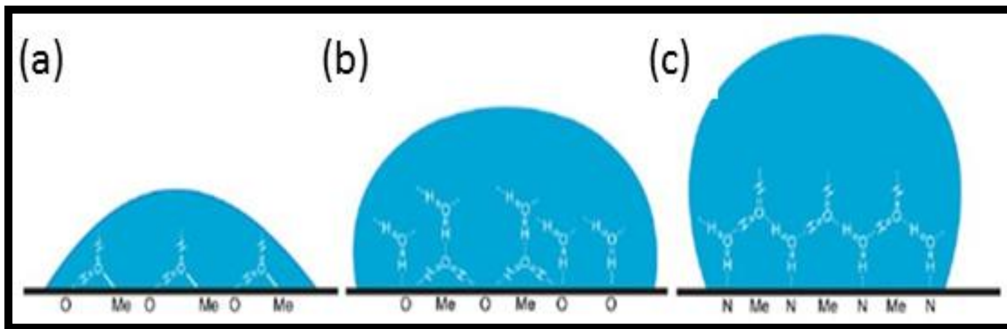

Figure 1.3.2 Orientation of water molecule on the surface of (a) high-electronegativity metal oxide (b) low electronegativity metal oxide (c) low electronegativity metal nitride. [29]

Another study done by Daniel J. Preston et al. reported that the REOs ceramics are intrinsically hydrophilic like every other oxide [30]. The group found that the WCA of the ceramic immediately after Argon plasma etching which is known to remove the atmospheric hydrocarbon contamination was ≈ 0˚. Temporal WCA measurements and XPS measurements showed that WCA increased as a function of hydrocarbon contamination on the surface to reach a value greater than 90˚ as

shown in figure 1.3.3. A decrease in surface free energy with time for the REO samples responsible for the increase in WCA was attributed to hydrocarbon adsorption on the surface. This study was also done on ceramic pellets. AFM scan shows roughness of pellet in several hundreds of nanometer.

Similar careful measurements of WCA on gold surface by removal of hydrocarbon contamination and oxide by Zisman et al. proved that gold surface is also intrinsically hydrophilic as opposed to the reports by Erb and Fowkes [31, 32].

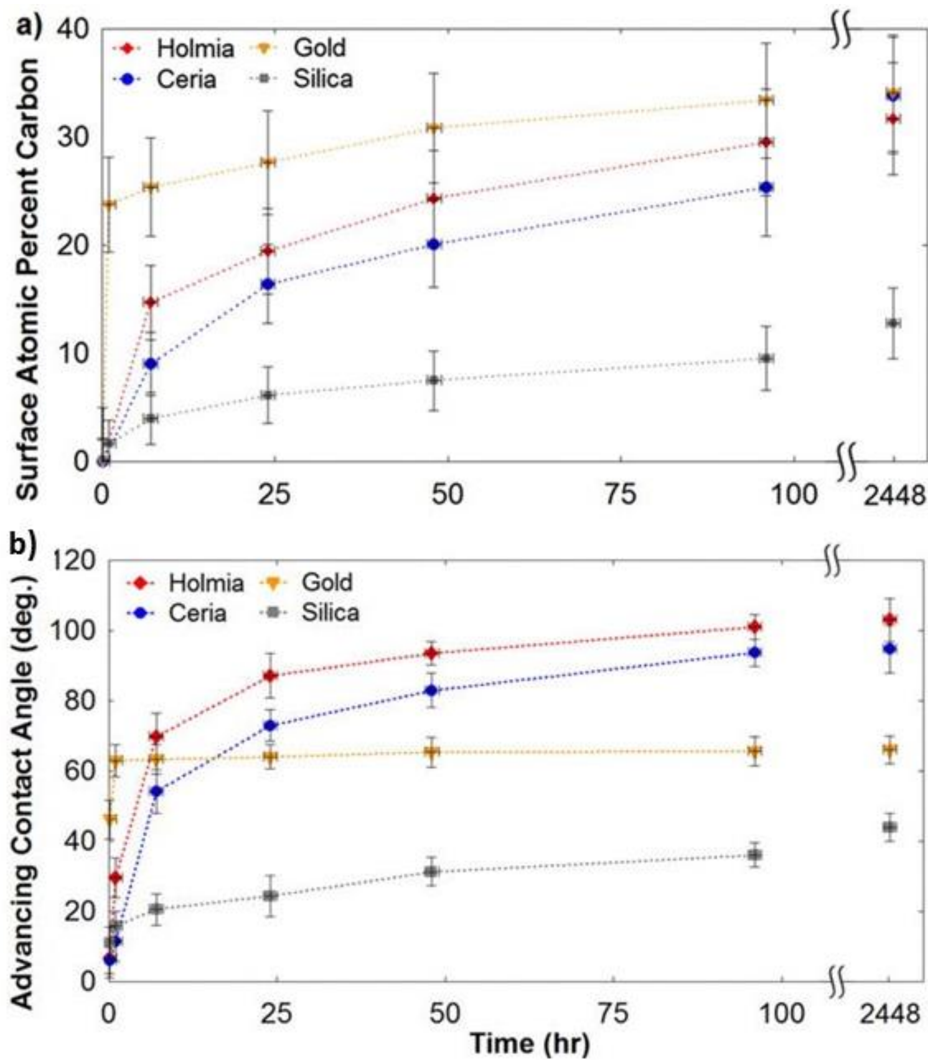

Figure 1.3.3 (a)Surface atomic percent of carbon as a function of time (b) Advancing WCA as a function of time[30]

Kripa K. Varanasi et al. demonstrated the role of surface stoichiometry on the wetting properties of REOs [33]. The group showed that a freshly sputtered film of ceria has a O/Ce ratio close to 3.3 and it undergoes relaxation in ultra-high vacuum environment until the ratio approaches 2.2 and the film becomes hydrophobic. The study showed that despite similar carbon contamination levels in sputtered ceria and alumina films former was hydrophobic (≈ 104˚) while latter was found to be hydrophilic (≈45˚). The findings suggested that the hydrocarbon contamination of the ceria sputtered films could not explain the unique hydrophobic behaviour of REOs. The carbon contamination comparison however drawn with the study done by Preston et al. is inappropriate as in both cases the nature of sample is different. It has already been known that for ceria the amount of hydrocarbon adsorption depends on the surface roughness [34]. Additionally, the XPS results also depend on surface roughness. The same group fabricated superhydrophobic surface (WCA=160˚) by laser texturing of a ceria pellet (WCA=102˚) [35].

Il-Kwon Oh et al. investigated the hydrophobicity of atomic layer deposited (ALD) REO thin films (Er_2O_3, Dy_2O_3, CeO_2, Y_2O_3 and La_2O_3) of different thickness on Si(100) using organic precursors [36]. The group showed that indeed these REO films of thickness greater than 50 nm in thickness were hydrophobic. They also reported the dependence of WCA of thin films on the thickness of the film suggesting the effect of substrate underneath the film with decreasing film thickness. ALD process involves organic precursors. Hence, it is not a very clean process unlike PLD and sputtering where the films are grown in vacuum. Control

over carbon contamination on the surface of the film is difficult, if not impossible. The crystallinity of the films prepared has not been discussed.

An extensive literature survey shows that there is a wide scatter in the reported WCA values for thin films of the same oxide. Some of these studies have even claimed the reported WCA value to be intrinsic to the oxide. However, these studies have overlooked several factors that affect the measured WCA namely roughness, surface contamination, grain boundary, adsorbed species etc. In this study our focus is to elimnate as many of these factors as possible by using Pulsed Laser Deposition method to grow oxide films of very good quality (preferably single crystalline) so that we can access the intrinsic WCA. Pulsed Laser Depostion is a vacuum deposition technique and hence it is an ideal method for preparation of contamination free surfaces.We will also evaluate our protocol for measurement in terms of reproducibility and scatter.

The origin of hydrophobicity of REOs is not clear. There have been conflicting reports about the same. The hydrophobic nature makes it a potential replacement for gold in heat exchange systems as it promotes dropwise condensation. In this study, we will investigate the intrinsic WCA value for REOs to improve the understanding of the origin of its claimed hydrophobicity.

The dependence of WCA on the thickness of the film has not been studied so far. Hence, the effect of the underlying substrate on the WCA constitutes an interesting problem to explore.

CHAPTER 2

METHODS

2.1 THIN FILM FABRICATION (PULSED LASER DEPOSITION)

Pulsed Laser Deposition (PLD), which is a physical vapour deposition technique has been used to prepare thin films in this study. The technique involves the use of a high power nanosecond laser pulse which is tightly focused onto a spot onto the target surface. The laser pulse delivers an enormous amount of energy into a small region near the surface of the target causing the target material to ablate. The ablated material expands in a low pressure environment normal to the surface of the target to form a highly directional plasma plume. The substrate is placed in the path of the expanding plasma. The energetic species in the plasma get absorbed on the surface of the substrate to form adatoms and these adatoms diffuse around on the surface to a thermodynamically favored site and bond. The process parameters critical for the quality and uniformity of the deposited film are laser fluence (energy density), laser repetition rate, background gas pressure (generally oxygen for oxide growth), temperature of substrate and target substrate distance.

Smith and Turner were the first to prepare thin films in vacuum using a Ruby laser in the year 1965 [37]. But the successful preparation of stoichiometric thin films of a multi-component material like $YBa_2Cu_3O_7$ (high temperature superconductor) using pulsed excimer laser evaporation of a single bulk material target in vacuum by Venkatesan et al. at Bell Communications Research in the year 1987 established

the specific recipe for successful implementation of this process [38]. Since then it has been widely used for preparation of multi-elemental compound thin films such as oxide superconductors [39], metals [40], ferroelectrics [41], piezoelectrics [42], polymers [43] etc.. The versatility and speed of the process still remains unmatched [44]. It can be used to deposit a wide range of materials metal, semiconductors, oxides, nitrides etc. The conceptual and experimental simplicity and the ability to rapidly prototype films of complex materials are the most important reasons for its popularity in the study of thin films [45].

The PLD setup used in the study uses a KrF excimer laser (λ=248 nm) Compex Pro 110 manufactured by Lambda Physik. Pulse width is 15ns and laser repetition rate in the range 1-10 Hz can be used. The maximal output energy is 450 mJ. An optical mirror and lens system is used to direct the beam into the vacuum chamber wherein the laser beam is focused into a ~4.5mm^2 rectangular spot on the target. The vacuum chamber can be pumped down by a roughing pump and turbo pump connected in series to a vacuum of the order 10^{-8} Torr. The chamber consists of a target carousel which can hold a maximum of up to six targets simultaneously. The target during ablation can be rastered and rotated by motors controlled by a computer program. There is also a substrate holder with an integrated resistive heater which can be used to deposit at elevated temperatures up to 950˚C. Mass Flow Control system maintains the background gas pressure of pure O_2 and N_2 inside the chamber as required during deposition. The schematic of the PLD with RHEED and the Neocera manufactured PLD setup used is shown in figure 2.1.1 and 2.1.2 respectively.

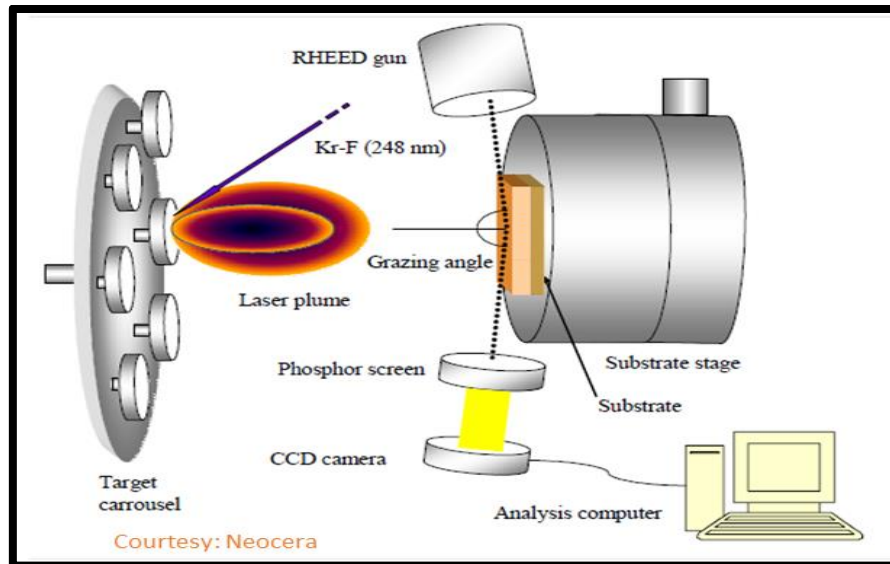

Figure 2.1.1 Schematic of PLD with RHEED

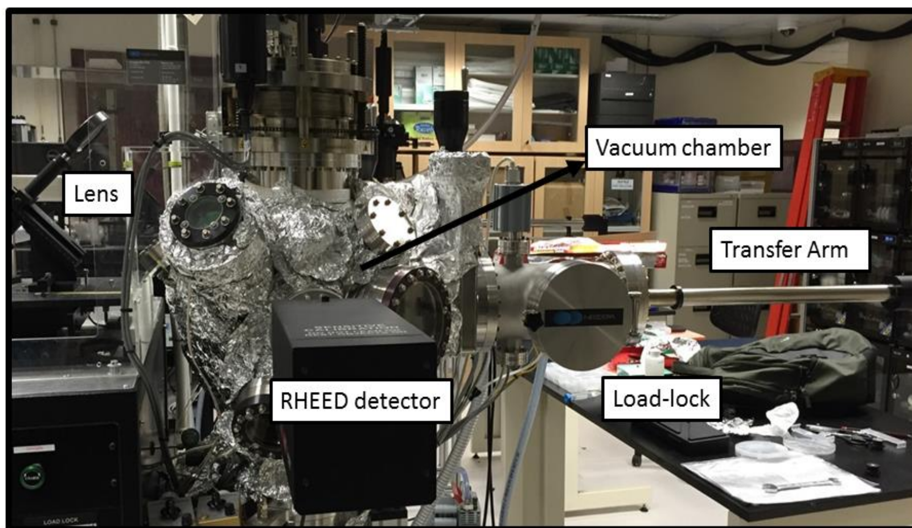

Figure 2.1.2 Neocera PLD setup

2.1.1 Target Preparation

The quality of the target is paramount in fabricating a high quality film by PLD. About 7 gm of each powder is taken in a cleaned mortar and pestle and is ground into finer particles. It is then transferred in a cylindrical die 1" in diameter and

pressed in a hydraulic press at 4200 psi for 30 minutes. The compact pellet is then sintered in a furnace at approximately $0.6T_m$ (T_m = melting point) for about 16 hours supported on an alumina crucible in a tube furnace.

2.1.2 Substrate Cleaning

The quality of the substrate is very important for growth of good quality thin films. All the substrates used in the study were purchased from CrysTec GmbH Company. These substrates were sonicated for 10 minutes in each Acetone, Ethanol and DI water successively to remove any surface contamination. The substrates were then blow dried with N_2 and mounted on the substrate holder plate with the help of silver paste.

2.1.3 Deposition Conditions

It was ensured before deposition that the base pressure was as low as ~E^{-8} torr in the vacuum chamber. A transfer arm and load-lock arrangement is used to load the substrate and target into the vacuum chamber. The desired background gas pressure of oxygen needed for deposition is maintained precisely by a mass flow controller (MFC) controlled by software. The next step is to increase the temperature of the substrate to the deposition temperature. A program can be written in the software with the set point values, holding time and ramp rates. Pre-ablation (about 3000 laser pulses) of the target is done prior to actual deposition with a shutter between substrate and target so as to get rid of any surface contaminants on the target. Once the desired temperature and pressure is reached, the energy of the laser beam just outside the window is measured. The desired laser parameters (number of pulses,

frequency and energy/voltage) are set and deposition is performed. The growth of film is in situ monitored using a high-pressure RHEED.

2.1.4 High-Pressure Reflective High Energy Electron Diffraction (RHEED)

It is an important tool in surface science to investigate the periodic arrangement of the surface atoms. The schematic for RHEED is shown in figure 2.1.3.

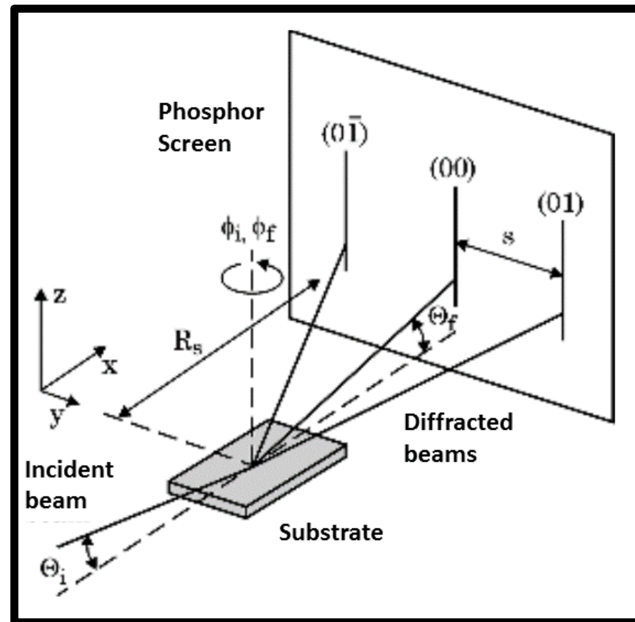

Figure 2.1.3 Schematic view of the RHEED geometry .Θ_I (Θ_F) and ϕ_I (ϕ_F) are the incident and azimuthal angles of incident(diffracted) beam. Rs is the distance between substrate and the phosphor screen and S the distance between the diffraction spot or streaks [46].

Monoenergetic electron beams having energy typically in the range 10-50 keV strike the sample surface at a grazing angle θ_i (< 3°). The beam has a very small component of wave vector perpendicular to the sample surface and a large wave vector parallel to the sample surface. RHEED hence is a surface sensitive tool. The incident beam component specularly reflected by the sample surface is indexed as

(0 0) reflection in figure 2.1.3. Some part of the electron beam get diffracted by the periodic arrangement of atoms on the surface and is steered left and right laterally. For the orientation of substrate shown in the schematic, we get (0 1) and ($0\,\bar{1}$) diffraction streaks. The lateral spacing S and the distance of the phosphor screen from the point of strike of the electron beam R_S are related by the Bragg condition for diffraction by the equation

$$\mathbf{d = R_s\lambda/S}$$

where d = spacing between plane of atoms and λ = De Broglie wavelength of electron beam.

The intensity of the specularly reflected electron beam varies during the film growth, depending on the mode of growth. Layer by layer growth (2D) will produce intensity oscillations wherein each peak signifies the completion of one monolayer. Island growth (3D) leads to increase in the roughness on the substrate and causes an overall decrease in RHEED intensity with progressive deposition. The RHEED pattern becomes spotty. Mixture of layer by layer and island growth is commonly observed in many heteroepitaxial thin film deposition. Here, the growth mode is initially layer by layer and later it changes to island growth mode. Damping of intensity oscillations is seen in this case and eventually oscillation ceases. Step propagation, or step-flow growth is a special growth mode in which the morphology of the substrates remains unchanged and the diffraction intensity stays constant. The different film growth modes discussed above are shown in figure 2.1.4.

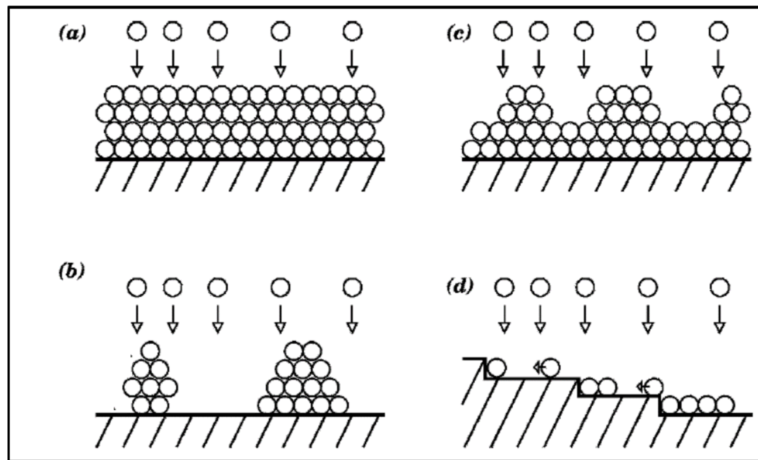

Figure 2.1.4 Film growth modes **(a)** Layer-by-layer, **(b)** Island growth, **(c)** mixed mode and **(d)** step flow[47]

RHEED needs a very high vacuum for operation which was a limitation for its use as an in situ growth monitoring technique in PLD. Most of the complex oxides were deposited in high background pressure of oxygen. This was overcome by the use of a two stage differential pumping system and the High-Pressure RHEED was developed [48, 49].

The intensity oscillations in the specularly reflected (0 0) spot observed in films which show layer-by-layer mode of growth (2D) is used for in situ monitoring of growth rate. The surface of substrate becomes rough progressively as the surface coverage (θ) increases to 50% and then roughness decreases up to completion of one monolayer. This is reflected in the intensity of specularly reflected spot and the intensity oscillates as shown in the figure 2.1.5. The same roughening and smoothening schedule repeats and oscillations are produced in the intensity during PLD. Generally, each oscillation corresponds to completion of a unit cell. Hence

with this technique, the films which show layer-by-layer (2D) growth can be controlled to the precision of unit cell.

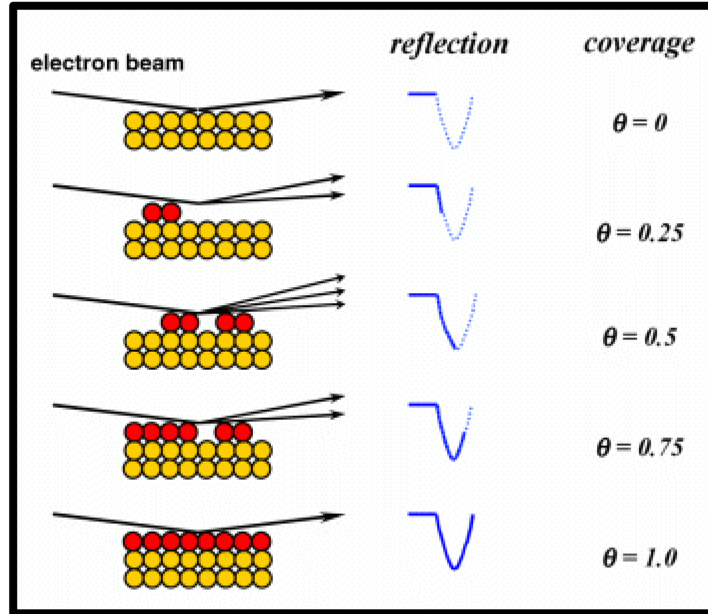

Figure 2.1.5 RHEED oscillations observed in layer-by-layer growth mode (*Courtesy : http://www.material.tohoku.ac.jp/*)

2.2 CHARACTERIZATION TECHNIQUES

2.2.1 X-Ray Diffraction (XRD)

It was in the meeting of German Physical Society in the year 1912 that Max von Laue announced the discovery of X-ray diffraction by crystals. S. V. Borisov and N. V. Podberezskaya have presented a brief account of the important developments in the field of X-ray Diffraction which made it such a useful technique for structural analysis of crystalline materials [50].

The X-ray spectrum includes wavelengths of the order of lattice spacing in crystalline materials. X-rays being electromagnetic wave get scattered on interacting with the electron cloud of the atoms in a crystal. This interaction is strong with the tightly bound electrons and weak with the electrons defined by a delocalized wave function.

Based on the spacing of lattice planes in the material the angular positions of the diffracted beam follows the very famous Bragg Equation.

$$n\lambda = 2d_{hkl}sin\theta$$

Where n is the order of diffraction, λ wavelength of X-ray, d_{hkl} is the spacing between the plane with miller indices h k l and θ is the half the diffraction angle.

Intensity of the diffracted beam is decided by the nature and distribution of atoms in the crystalline structure. The mathematical expression structure factor (F_{hkl}) decides the intensity of X-rays at an angular position indicated by Braggs Law.

$$F_{hkl} = \sum_{n=1}^{N} f_n e^{2\pi i(hu_n + kv_n + lw_n)}$$

Where f_n is atomic form factor, N is the number of atoms in the unit cell, (h k l) miller index of the plane and [u_n v_n w_n] is the coordinate of the atoms.

A typical laboratory X-Ray Diffraction machine consists of an X-ray tube which generates X-rays. The monochromatic beam of X-ray is directed towards the sample mounted on a stage. The detector and the source move simultaneously so as to maintain the angular relationship with the sample stage necessary for diffraction

as shown in figure 2.2.1. The detector records the intensity for the desired angular range and the spectrum is compared against database to identify the crystalline phase.

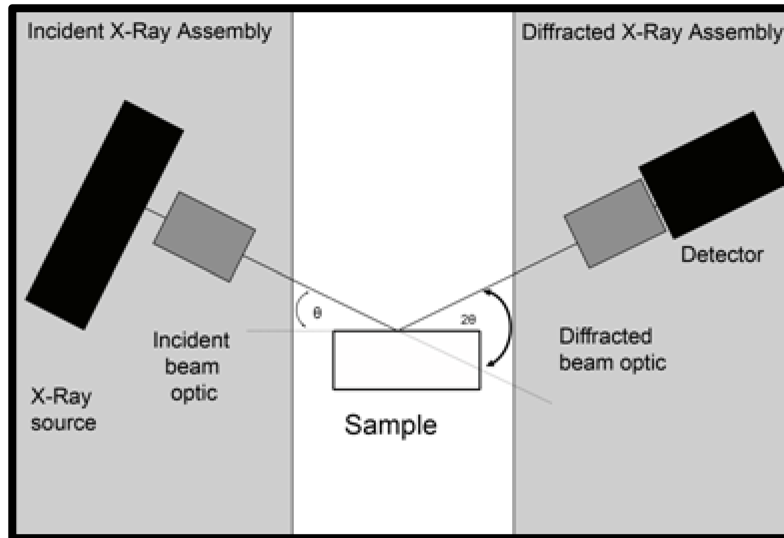

Figure 2.2.1 Schematic of a XRD setup

XRD study of thin film gives information regarding the phase of the film, crystal quality (single crystal, polycrystalline or amorphous), lattice parameters and the orientation relationship between the film and the substrate (if any).

In this work, all the XRD scans have been obtained with a Bruker D8 Discover instrument shown in figure 2.2.2. The X-Ray tube has a copper target and the monochromatic X-ray beam used is Cu K_α (1.54Å).

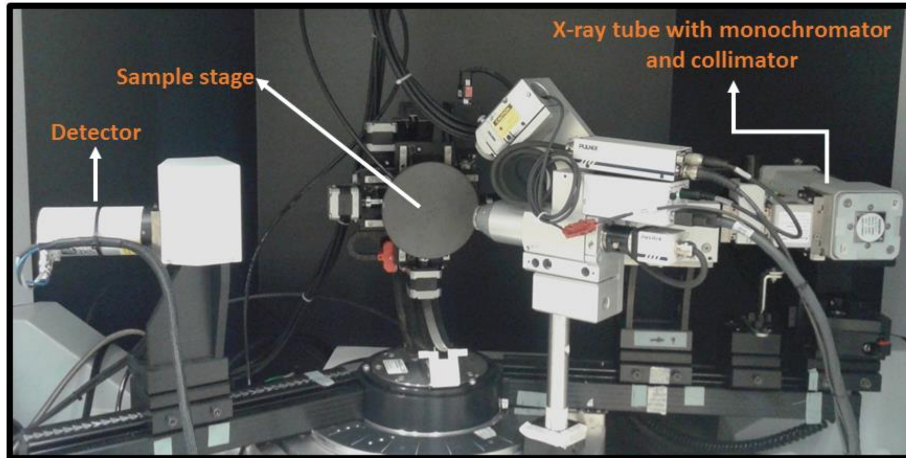

Figure 2.2.2 XRD setup Bruker D8 Discover

2.2.1.1 X-Ray Reflectometry (XRR)

It involves recording the intensity of the x-ray beam reflected by the surface of the sample at grazing angles. Typically a reflectivity spectra is recorded in the range 0° and 10° in 2θ. Density of the thin film can be determined from the critical angle (below which external reflection occurs) θ_c. The period of the interference fringes can be used to measure the thickness of the film and the slope of the reflectivity curve beyond the critical angle θ_c is a measure of the film roughness. A typical XRR spectrum is shown in figure 2.2.3.

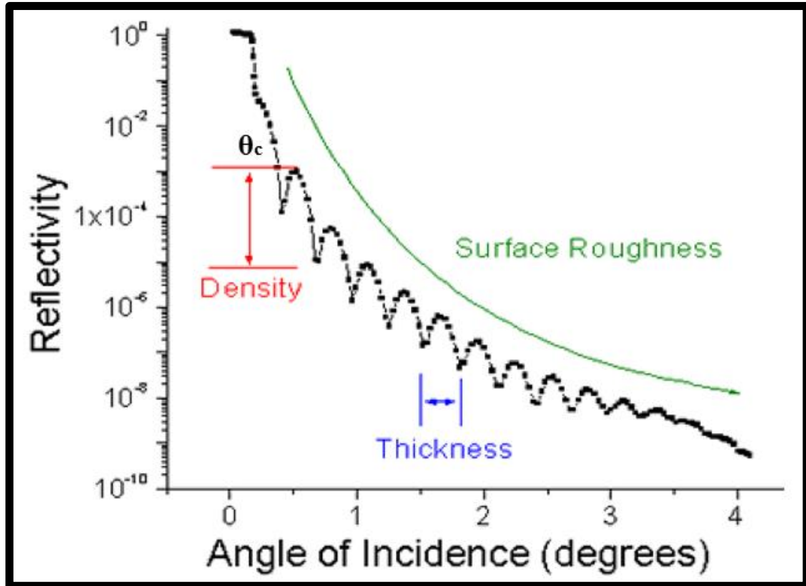

Figure 2.2.3 Typical XRR spectrum showing meaning of parameters.

In this study, it has been used primarily for measurement of film thickness for evaluating growth rate of different oxides. The experimental reflectivity is fitted against simulated curve by a software Leptos to get the values for film thickness, roughness and density.

2.2.2 Atomic Force Microscopy (AFM)

AFM was invented in the pursuit to extend the Scanning Tunneling Microscopy (STM) technique to investigate surfaces of electrically non-conductive materials by Binnig and Quate in the year 1986 [51].

AFM is a scanning probe microscopy technique which is most widely used to study the surface morphology of substrates and deposited thin films. It is very simple to operate unlike TEM or SEM. AFM uses the Van Der Waals interaction between a very sharp tip (typically 5-20 nm) mounted on a cantilever and the sample surface

to probe surface topography. The tip sample interaction can be understood mathematically by the famous Lennard-Jones potential equation which approximates the interaction between a pair of neutral atoms or molecules. Figure 2.2.4 shows the equation and the potential curve.

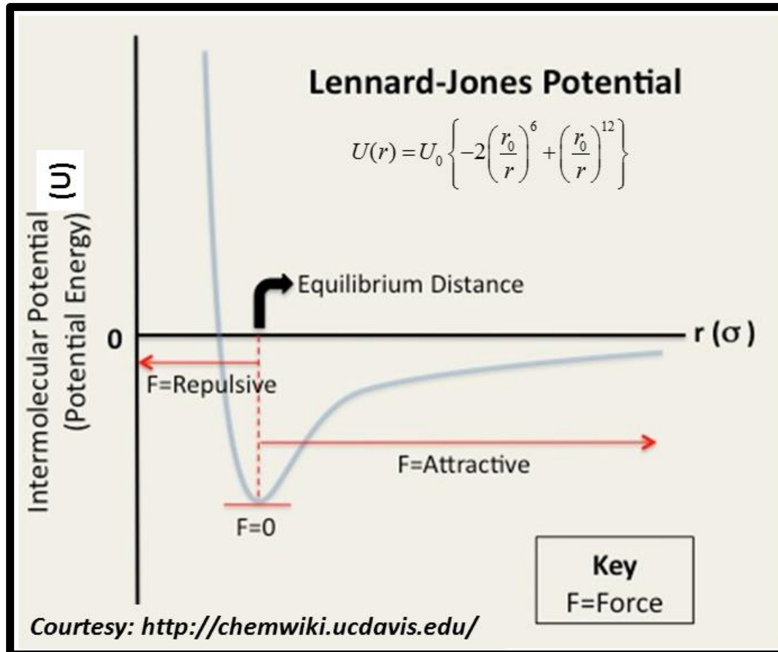

Figure 2.2.4 Lennard-Jones Potential Curve

A typical AFM has a sample stage, a laser diode, a photodetector, a cantilever with a tip (probe) and a feedback control unit. The laser from the source is reflected from the back of the tip towards the 4 – quadrant photodetector. During initial alignment, the reflected laser spot is directed to the centre of the photodetector. The tip scans the area of interest by breaking it into lines and breaking each line into points. Depending on the surface topography, the cantilever tip bends away or toward the sample due to which the reflected laser spot moves away from the centre of the four

quadrant photodetector. The amount by which a cantilever bends depends on its spring constant. The feedback unit accordingly moves the sample stage closer or further to the tip to bring the reflected laser spot back to the centre of photodetector. Thereby, a surface topography image of the sample is generated from the photodetector signal.

There are three operating modes of operation of an AFM which can be bunched into two categories – static and dynamic

Static mode

1. Contact mode AFM

The imaging is performed while the tip is in close contact with the sample and hence is in the repulsive force regime. The short-range repulsive forces are balanced by Van der Waals attractive force. This mode is used to study surface topography and adhesion physics on relatively hard surfaces which are not influenced by the direct contact of the tip. This mode cannot be used to produce atomic resolution images.

Dynamic mode

In this mode of operation, the cantilever tip is made to oscillate near resonant frequency (typically between 5-400 KHz). An additional piezoelectric element is used for the job. The cantilever tip oscillates near resonant frequency and scans the sample. The reflected laser spot from the back of the tip also oscillates with the same frequency and some amplitude. Due to the surface topography of the sample surface, the tip sample interaction force changes causing the amplitude of the oscillation of the reflected laser spot to change. The feedback unit in turn moves

the sample stage closer or further to the sample to maintain the initial set amplitude. This signal is used to produce surface topography images. Figure 2.2.5 shows the schematic of an AFM operating in tapping mode.

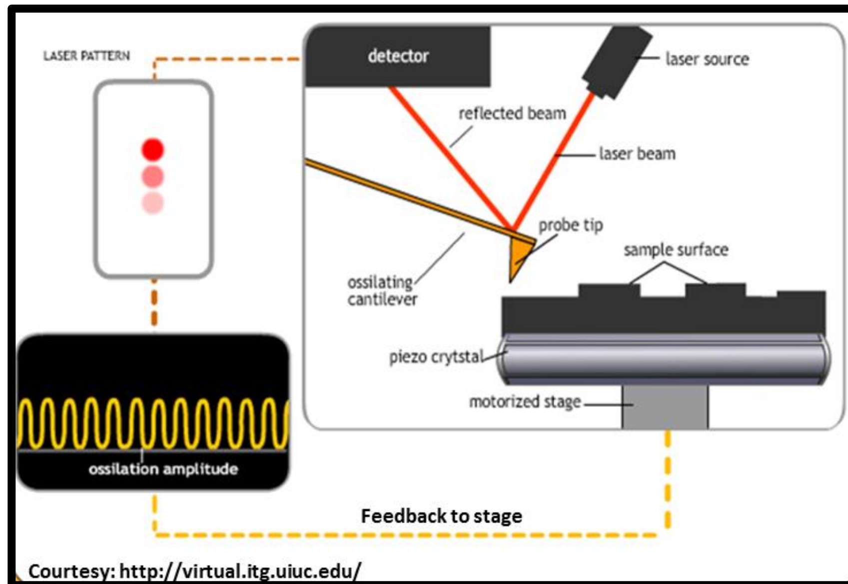

Figure 2.2.5 Schematic AFM operation in tapping mode.

2. Non-Contact mode AFM

Non-contact mode was developed by Martin et al. in the year 1987 to image soft biological samples [52]. The oscillation amplitude of the cantilever tip is small in this mode and the tip remains close to the sample surface but never touches the sample.

3. Tapping mode AFM

Tapping mode AFM was introduced by Zhong et al. in the year 1993. They used an oscillating tip in the vicinity of the sample with an amplitude of up to ~100 nm and generated reproducible images of the surface topography [53].

In this mode the amplitude of oscillations is such that the tip touches the sample and moves completely away from the sample in each oscillation cycle.

In this study, all the AFM topographic images have been recorded in tapping mode with Agilent Technologies 5500 AFM. Figure 2.2.6 shows the AFM setup used for the study.

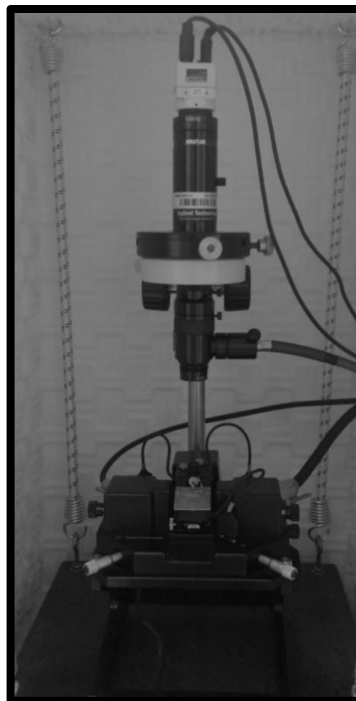

Figure 2.2.6 AFM setup.

2.2.3 X-Ray Photoelectron spectroscopy (XPS)

XPS also known as Electron Spectroscopy for Chemical Analysis (ESCA) was developed in 1960s by Kai Segbahn et al. in Sweden. It is a semi-quantitative technique for determination of surface chemistry. XPS is very surface sensitive as the photoelectrons are emitted typically from the top 1-10 nm of the sample being analyzed.

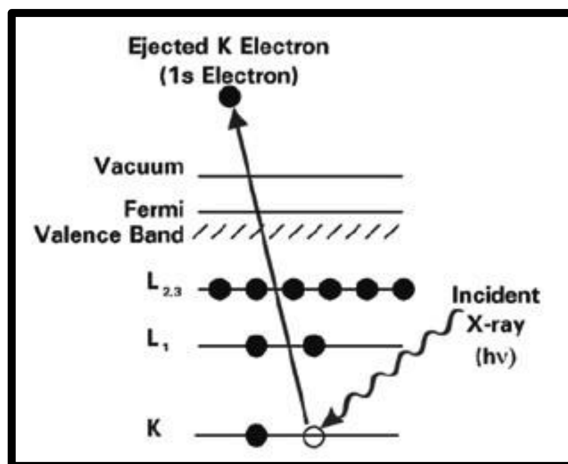

Figure 2.2.7 Photoemission Process for XPS analysis.

(Courtesy : http://xpssimplified.com/)

This technique uses a beam of monochromatic soft X-rays (generally Al K_α or Mg K_α) to knock out electrons from the core levels of an element on the surface of the sample as shown in figure 2.2.7. The kinetic energy of the photoelectron depends on the energy of the X-ray photon (hυ) and the binding energy (BE) of the electron.

$$KE = \hbar\nu - BE$$

Binding energy of the electron depends on the element from which the electron is knocked out, the orbital of the element from which it is knocked out and finally on the chemical environment of the element. These kinetic energies of the photoelectrons generated is used for the identification of the elements. The relative concentration of different elements present on the surface of the sample can be determined from the counts of photoelectrons. Any variation from the binding energies, or chemical shifts in the spectrum is used to obtain information on chemical states of an element.

In this work, XPS were performed using Axis Ultra DLD (Delay Line Detector) manufactured by Kratos Analytical shown in the figure 2.2.8. XPS spectra were recorded using Al-K_α X-rays (1489.6 eV, line width 0.85 eV), the energy scale of the spectrometer has been caliberated with standard Ag $3d_{5/2}$ samples, and the pressure in XPS analysis chamber was ~1xE-8 torr. The position of the C1s peak (with B.E. 285 eV) was used for charge correction of spectra as the samples were insulating.

Figure 2.2.8 XPS instrument**.**

2.3 WATER CONTACT ANGLE (WCA) MEASUREMENT

Water contact angle (WCA) is the central property that is representative of the interaction of a solid surface with water. As described before, WCA is the angle between the tangents to the water-air interface and to the solid surface at the line of

contact between the three phases. It is measured by convention on the liquid side as shown in the figure 2.3.1[9].

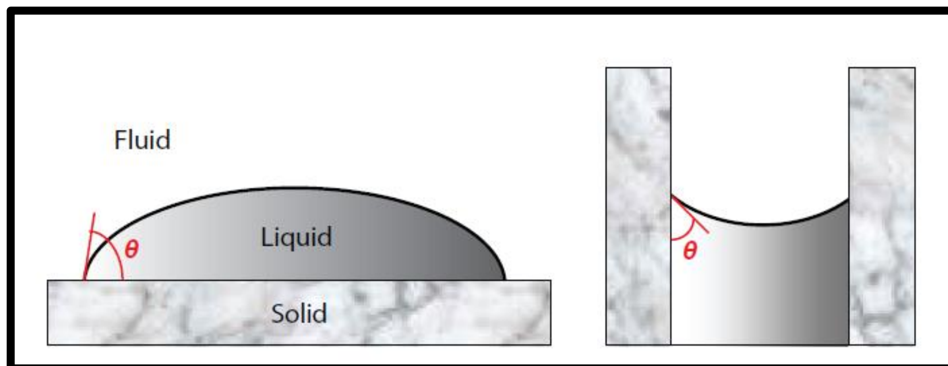

Figure 2.3.1 Schematic for contact angle θ

In this study, WCA has been measured by sessile drop method. The Dataphysics instrument used in the study is shown in figure 2.3.2.Water contact angle (WCA) is measured by image analysis of the drop dispensed on the sample (using a syringe, needle and microfluidic pump). The drop profile is curve-fitted and the angle is determined at the three phase contact line.

DI Water with resistivity of 18.2 MΩ.cm was used for recording WCA. Volume of droplet used for each measurement is 2μl. For each sample, WCA was measured 5 times successively. After each measurement, the drop resting on the film surface was blown off by N_2 and the sample was allowed to stabilize for 5 minutes before recording WCA again.

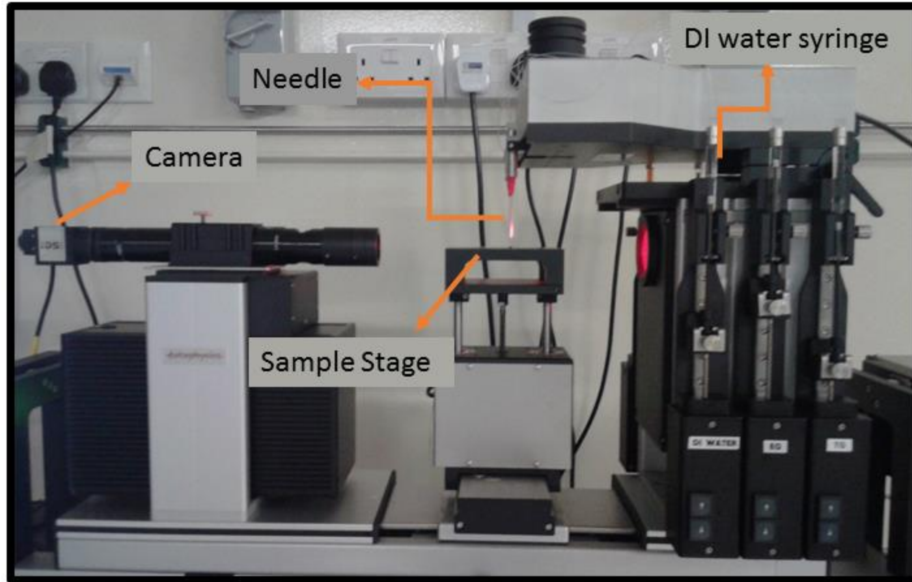

Figure 2.3.2 Dataphysics setup for WCA measurement.

CHAPTER 3

FILM FABRICATION AND CHARACTERIZATION

3.1 PULSED LASER DEPOSITION (PLD)

Lutetium oxide (Lu_2O_3) target was prepared from 99.9% pure powder supplied by Alfa Aesar. The target was sintered at 1500˚C. The YSZ (001) substrates were cleaned by the procedure discussed in methods.

A few trial depositions and subsequent characterization (AFM and XRD) were done to identify the ideal growth conditions for Lutetium oxide films on YSZ (001) substrates shown in table 3.1.1.

Table 3.1.1 PLD growth parameters

Parameter	Value	Units
O_2 pressure	1	mtorr
Substrate temperature	800	˚C
Laser fluence	~1.8	J/cm^2
Spot size	4.5	mm^2
Repetition rate	2	Hz
No. of laser pulse	4000	shots
Base pressure	~1xE-7	torr

3.2 REFLECTIVE HIGH ENERGY ELECTRON DIFFRACTION (RHEED)

In situ monitoring during growth was done using RHEED. The constants for RHEED set up were calculated using known STO (001) substrates with lattice parameter of 0.39 nm. It was found that the lateral separation of the spots on both sides of the (00) spot roughly corresponds to lattice parameter of YSZ substrate 0.514 nm as shown in the figure 3.2.1(a).

RHEED oscillations were observed as shown in figure 3.2.1(e) which is indicative of layer-by-layer (2D) growth. It took 28 laser pulses for the completion of one oscillation. The streaky pattern observed during different stages of deposition shown in figure 3.2.1 (b)-(d) also indicates that heteroepitaxial growth of Lutetium oxide takes place on YSZ (001) substrates. The streak which appears midway corresponds to the lattice parameter of cubic lutetium oxide 1.04 nm which is approximately twice the lattice parameter of YSZ (001) substrate. The mismatch is only about 1%. The in plane orientation relationship is $[100]_{Lu_2O_3} \parallel [100]_{YSZ}$.

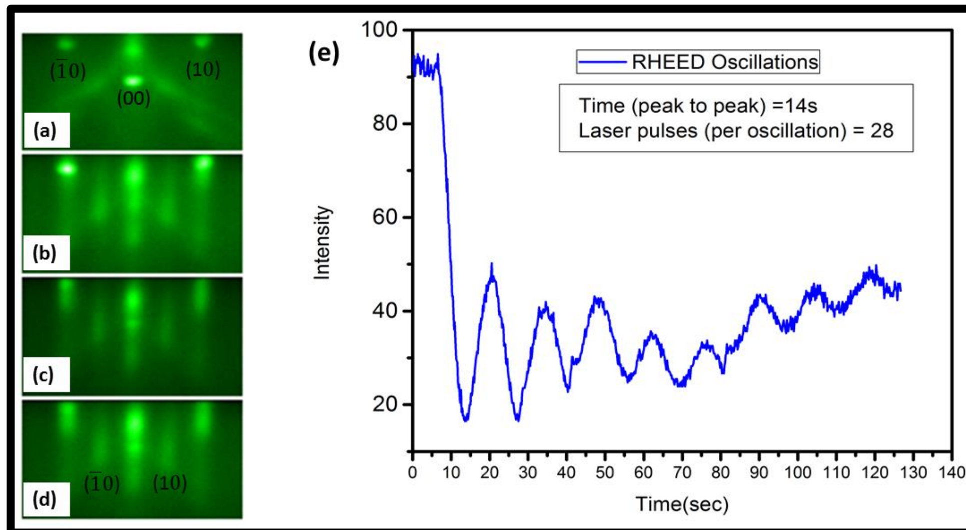

Figure 3.2.1 RHEED pattern (a) YSZ substrate before deposition, (b) after 1000 laser pulses, (c) after 2000 laser pulses and (d) after 4000 pulses. (e) RHEED oscillations of the specularly reflected spot during deposition.

3.3 X-Ray Reflectometry (XRR)

XRR was done for the Lu_2O_3 film prepared and the reflectivity plot is shown in figure 3.3.1. The thickness of the film was calculated by the spacing between the oscillations and also by the simulation software Leptos to be 37.5 nm.

Growth rate of Lu_2O_3

$$1 \text{ u.c.} \approx 1.039 \text{ nm}$$

$$\text{Growth rate} \approx 4000/37.5 \text{ shots/nm}$$

$$\approx 107 \text{ shots/nm}$$

$$\approx 111 \text{ shots/ u.c.}$$

It was seen in the previous section that 4 RHEED oscillations were observed in 112 laser pulses. Hence, it takes 4 RHEED oscillations (112 shots) for deposition of 1 u.c. thick Lu_2O_3 film on YSZ (001) with the deposition parameters used.

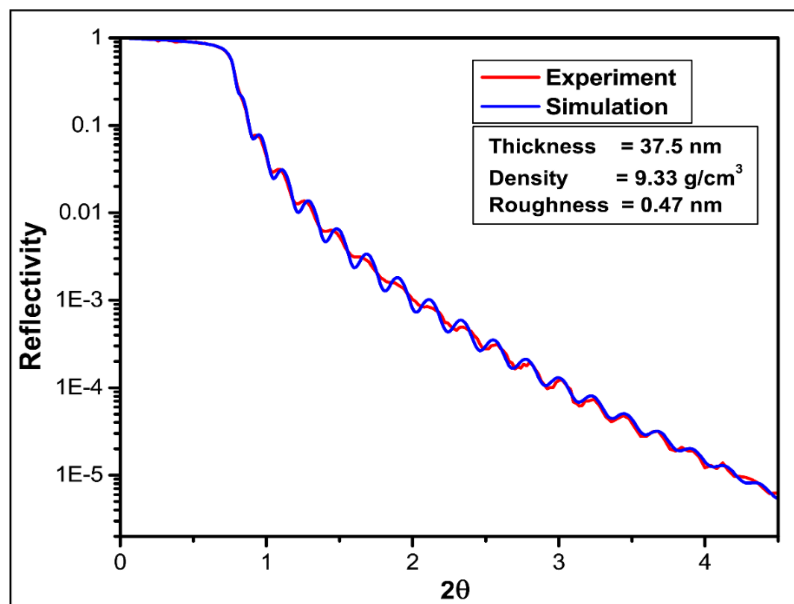

Figure 3.3.1 Reflectivity plot for lutetium oxide thin film

3.4 X-RAY DIFFRACTION (XRD)

The structure of bulk lutetium oxide is cubic with a lattice parameter of 10.39 Å as shown in schematic figure 3.4.1. The XRD scans for the Lu_2O_3 film are shown in figure 3.4.2.The 2θ position for the peaks corresponds well with the (0 0 *l*) lattice planes of the film and substrate. The out-of-plane orientation relationship between the film and substrate is hence $(001)_{Lu2O3} \parallel (001)_{YSZ}$. The d-spacing for the (001) plane of lutetium oxide film is slightly elongated ~10.50 Å. The effective structure of lutetium oxide in the film due to epitaxial strain becomes tetragonal.

The rocking curve (figure 3.4.2 (b)) for (004) peak of the film is ~0.33˚ indicating good crystallinity of the film. Also, the Φ scan for family of plane (figure 3.4.2 (c)) for the film shows only four equally spaced peaks (separation 90˚) which is consistent with the 4-fold symmetry of the resulting tetragonal structure of lutetium oxide film. XRD analysis shows that the film is single crystal with the epitaxial relationship $(001)_{Lu2O3} \parallel (001)_{YSZ}$.

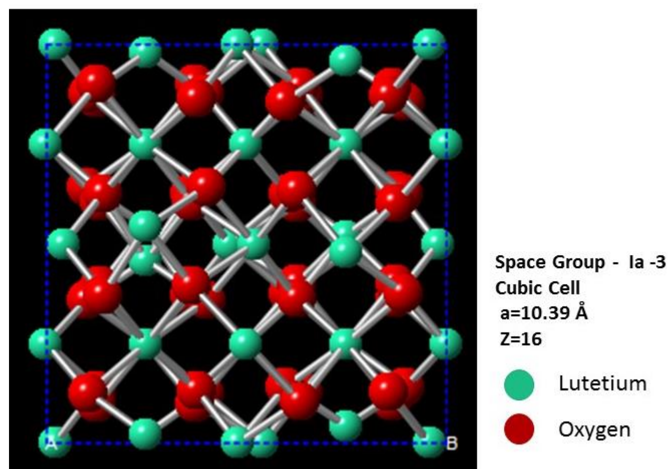

Figure 3.4.2 Schematic of Lu_2O_3 unit cell and crystal structure information.

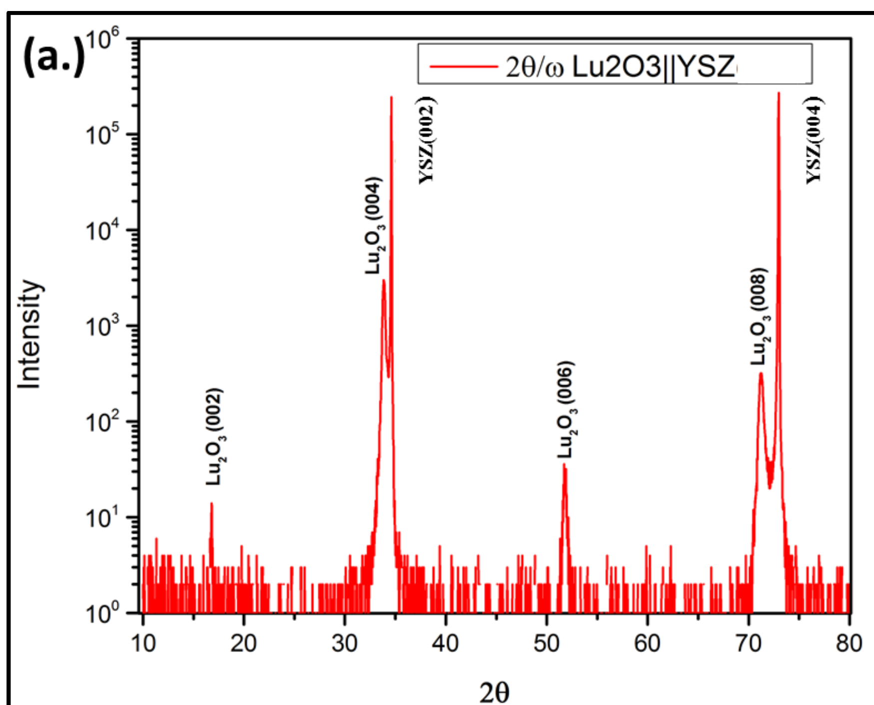
(a.)
2θ/ω Lu2O3||YSZ
Intensity
2θ
Lu_2O_3 (002)
Lu_2O_3 (004)
YSZ(002)
Lu_2O_3 (006)
Lu_2O_3 (008)
YSZ(004)

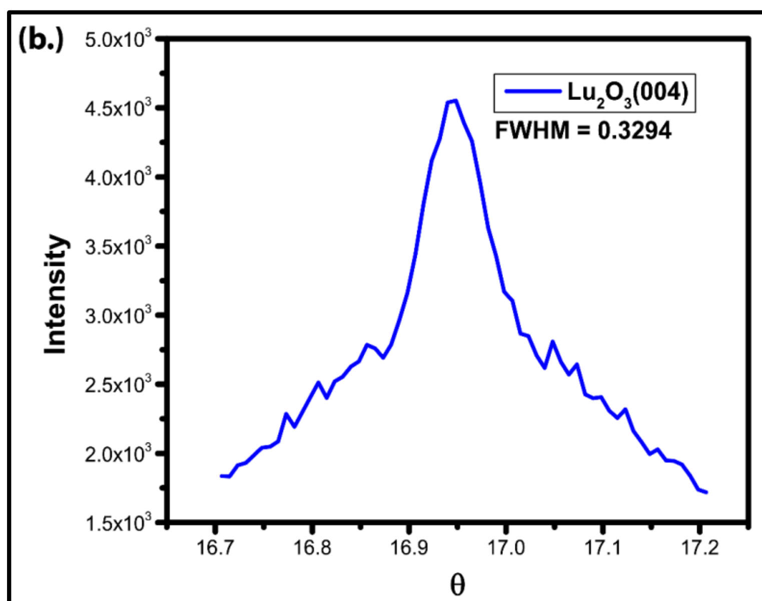
(b.)
Lu_2O_3(004)
FWHM = 0.3294
Intensity
θ

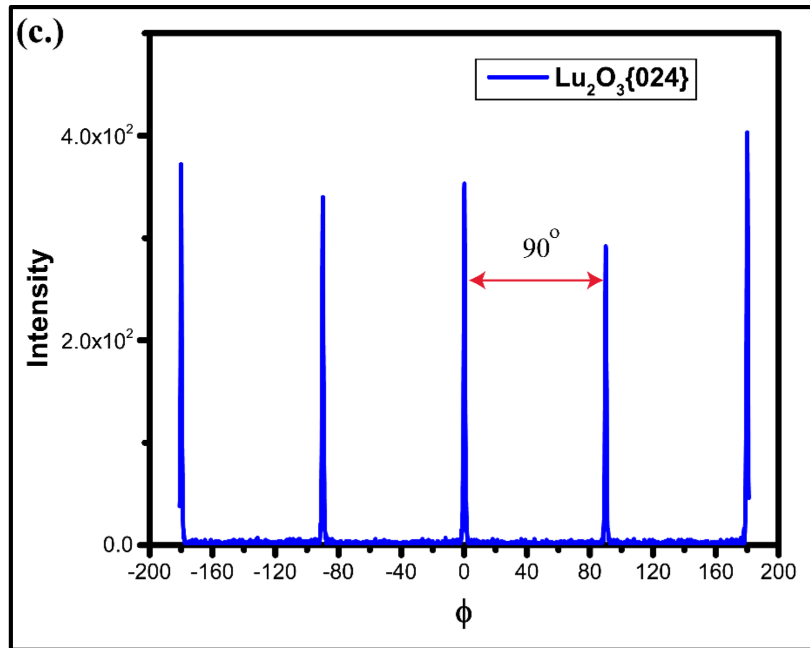

Figure 3.4.2 (a) 2θ/ω plot (b) (004) rocking curve (c) (024) Phi scan of lutetium oxide film

3.5 ATOMIC FORCE MICROSCOPY (AFM)

Figure 3.5.1 shows the AFM scan for the YSZ substrate and the lutetium oxide film. The roughness (rms) value is indicated above the AFM images. The Lu_2O_3 films are very smooth with rms roughness 0.16 nm.

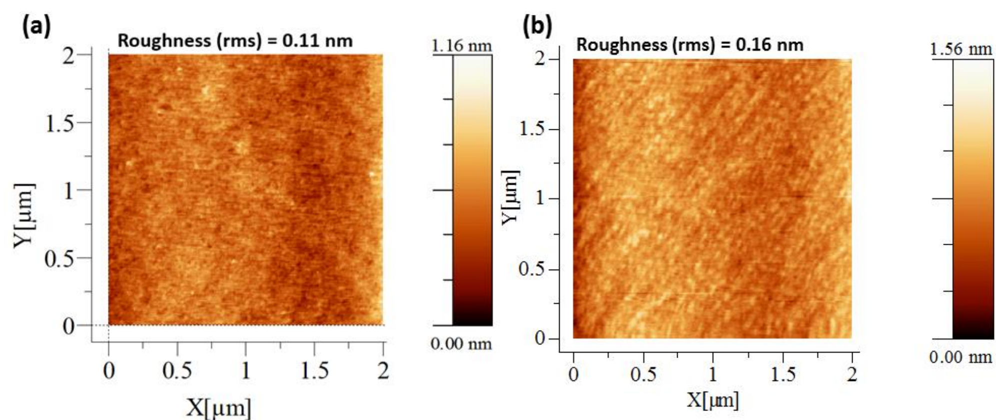

Figure 3.5.1 AFM scan image (a) YSZ (001) substrate (b) Lu_2O_3 film.

Similar characterization was done for Er_2O_3 and TiO_2. The data has been shown in Appendix A2.

3.6 CONCLUSION

Successful layer-by-layer (2D) growth of Lu_2O_3 (001) and Er_2O_3 (001) films on YSZ (001) was achieved using PLD. TiO_2 (001) single crystalline films were successfully prepared on STO (001) substrates by PLD. However, layer-by-layer growth could not be achieved for TiO_2.These films are single crystalline and are very smooth. The films are chemically homogeneous and smooth. Hence, it is an ideal solid surface for measurement of intrinsic WCA [9]. There is no contact angle hysteresis on ideal solid surfaces and hence the experimentally measured contact angle is Young's contact angle i.e. intrinsic WCA when the fluid is water [6].

CHAPTER 4

WATER CONTACT ANGLE (WCA)

4.1 REO SERIES

Thin films of oxides of rare-earth elements Lutetium, Ytterbium, Thulium, Erbium, Holmium, Dysprosium, Europium and Cerium were prepared using PLD. The films fabrication and characterization details are given in appendix A1.

The thickness of these films was measured roughly using a Bruker profilometer by placing a silicon substrate adjacent to the YSZ (001) with a mask. The thickness for all these films was found to be in the range 200-400 nm. These REO films were immediately transferred into a vacuum desiccator from the PLD vacuum chamber. The samples were stored for a period of about 6 weeks and the WCA was measured. The measured WCA angle values are shown in figure 4.1.1. The average of first five WCA is shown with error bars.

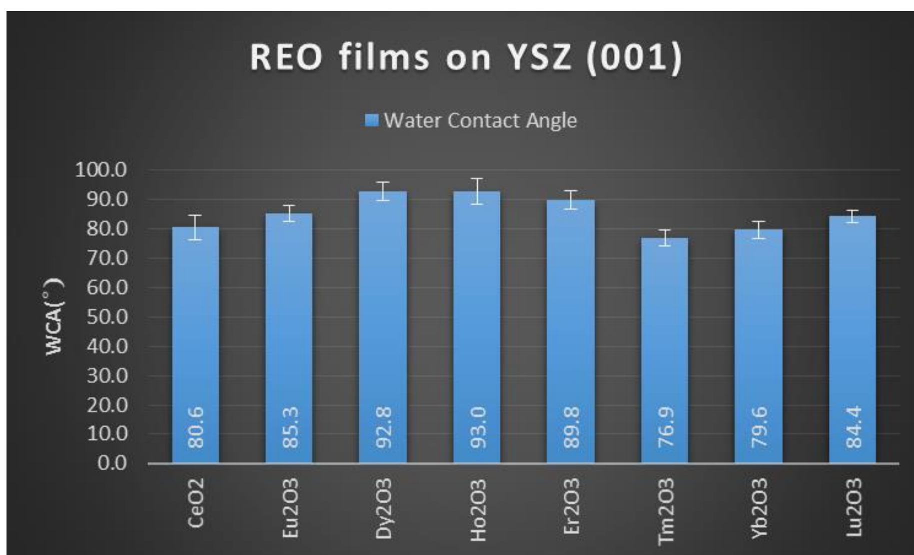

Figure 4.1.1 WCA for REO thin films on YSZ

4.2 TEMPORAL STUDY OF WCA OF OXIDE THIN FILMS

As per the growth rates calculated for Lu_2O_3 and Er_2O_3 discussed in the previous chapter and in appendix A2, thin film of thickness ~2 u.c, ~10 u.c. and ~ 50 u.c. of both oxides were grown on YSZ(001) substrates to investigate thickness dependence of WCA and influence of substrate on WCA of thin films. WCA was measured immediately after taking out the sample from the PLD vacuum chamber. This WCA is the intrinsic WCA for the oxide thin film free from any atmospheric contamination. Subsequent WCA measurements were done after different intervals of time. The very first measurement done on the sample is referred to as 1st WCA in this study.

WCA for Lu_2O_3 films, Er_2O_3 films and TiO_2 film is shown in figure 4.2.1.

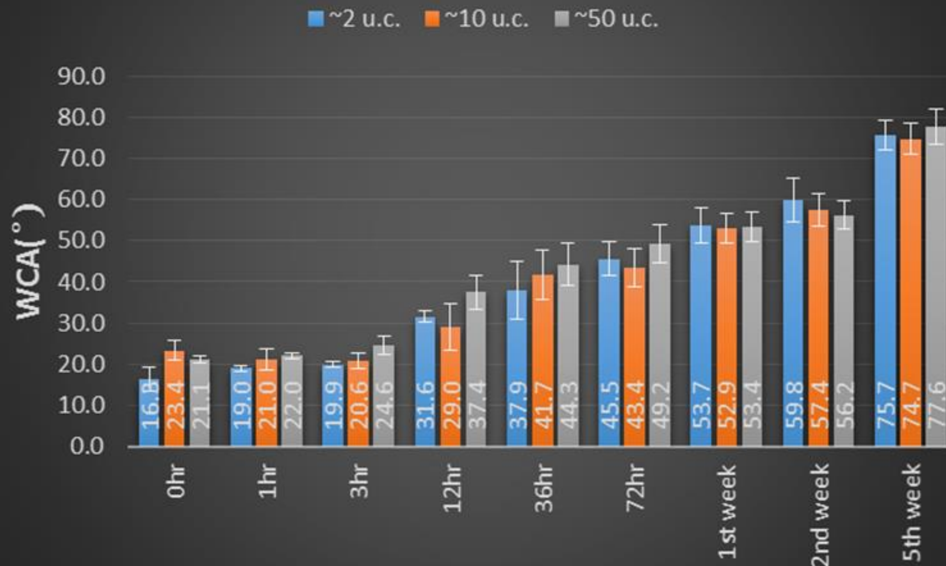
(a) Lu_2O_3 (001) films on YSZ(001)
~2 u.c.
~10 u.c.
~50 u.c.
WCA(°)
90.0
80.0
70.0
60.0
50.0
40.0
30.0
20.0
10.0
0.0
16.8 23.4 21.1
19.0 21.0 22.0
19.9 20.6 24.6
31.6 29.0 37.4
37.9 41.7 44.3
45.5 43.4 49.2
53.7 52.9 53.4
59.8 57.4 56.2
75.7 74.7 77.6
0hr
1hr
3hr
12hr
36hr
72hr
1st week
2nd week
5th week

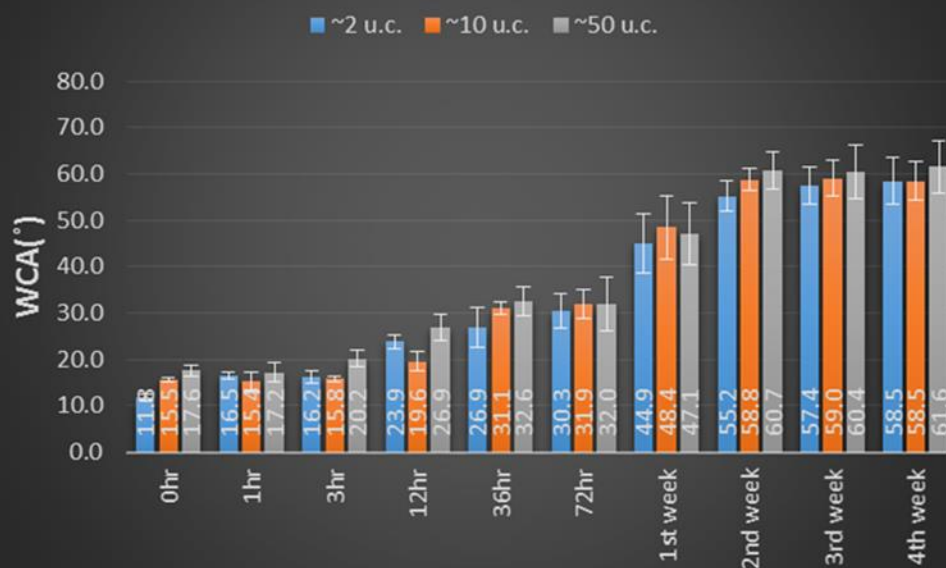
(b) Er_2O_3 (001) films on YSZ(001)
~2 u.c.
~10 u.c.
~50 u.c.
WCA(°)
80.0
70.0
60.0
50.0
40.0
30.0
20.0
10.0
0.0
11.8 15.5 17.6
16.5 15.4 17.2
16.2 15.8 20.2
23.9 19.6 26.9
26.9 31.1 32.6
30.3 31.9 32.0
44.9 48.4 47.1
55.2 58.8 60.7
57.4 59.0 60.4
58.5 58.5 61.6
0hr
1hr
3hr
12hr
36hr
72hr
1st week
2nd week
3rd week
4th week

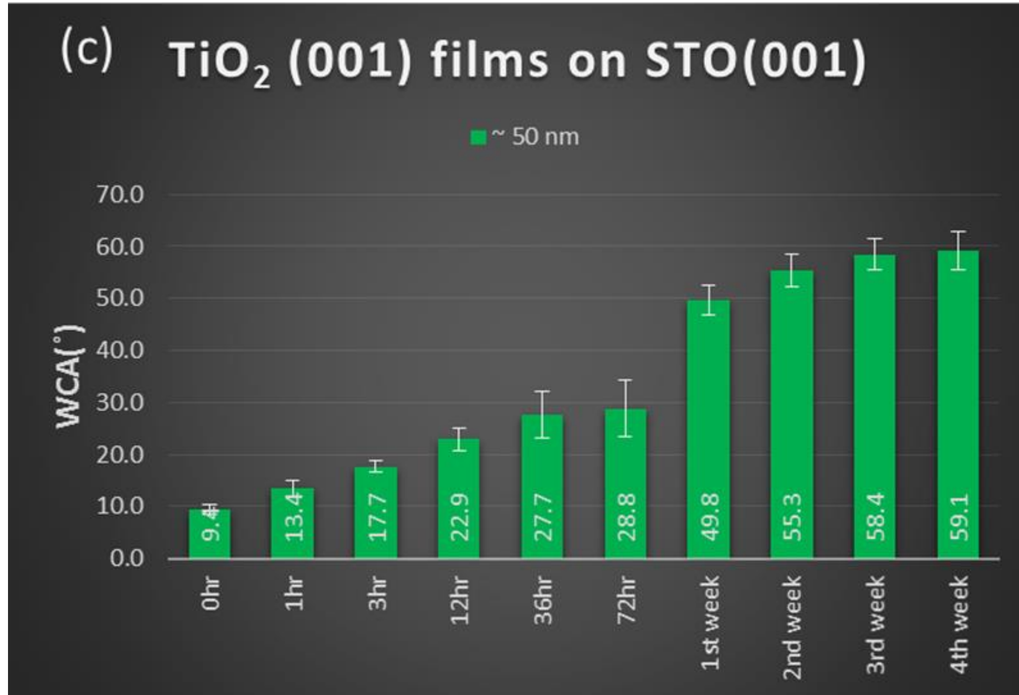

Figure 4.2.1 Average WCA for (a) Lu_2O_3 (b) Er_2O_3 films of different thickness (c) TiO_2 (~50nm) film.

WCA increases from a very low hydrophilic value for all the films and increases as the time exposed to ambient atmosphere increases. The ~2 u.c. film of both Lu_2O_3 and Er_2O_3 show a lower WCA than the thicker films when measured immediately from the chamber. WCA for TiO_2 film is lower than the REO films measured immediately from PLD vacuum chamber.

Temporal evolution of 1st WCA is shown for different films in figure 4.2.2. The nature of the temporal curve is similar for all the oxide films.

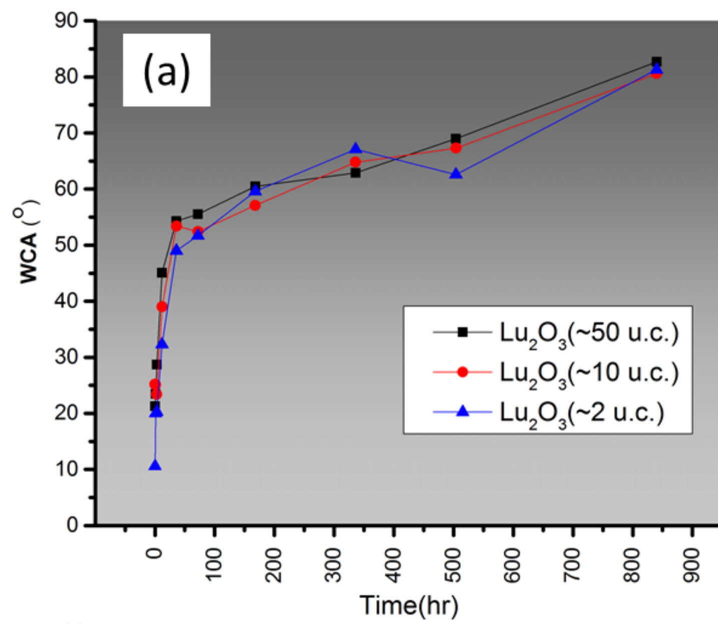
(a)
WCA (°)
Time(hr)
Lu_2O_3(~50 u.c.)
Lu_2O_3(~10 u.c.)
Lu_2O_3(~2 u.c.)
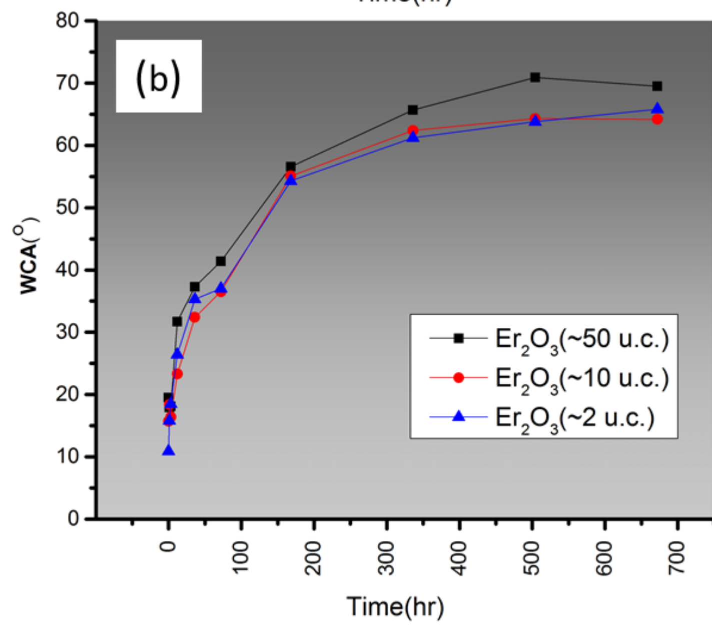
(b)
WCA(°)
Time(hr)
Er_2O_3(~50 u.c.)
Er_2O_3(~10 u.c.)
Er_2O_3(~2 u.c.)

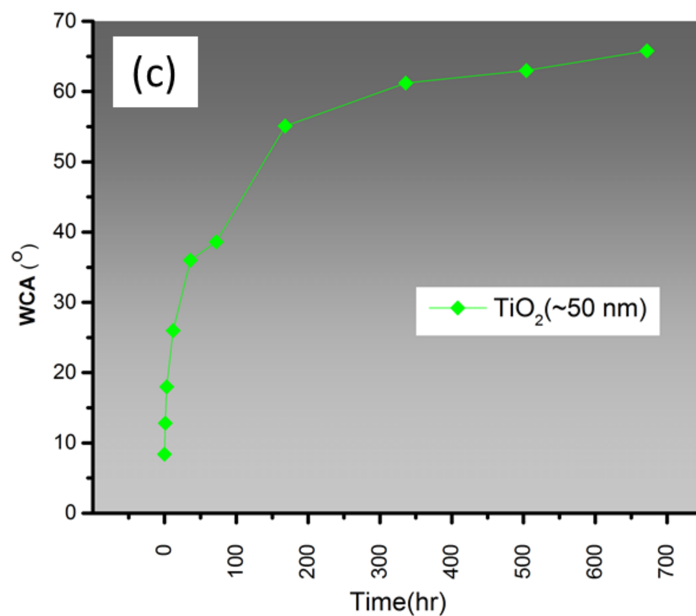

Figure 4.2.2 1st WCA of (a) Lu_2O_3 films (b) Er_2O_3 films and (c)TiO_2 film

The images for droplet shape on ~50 u.c. Lu_2O_3 film at different stages of exposure to ambient atmosphere is shown in figure 4.2.3.

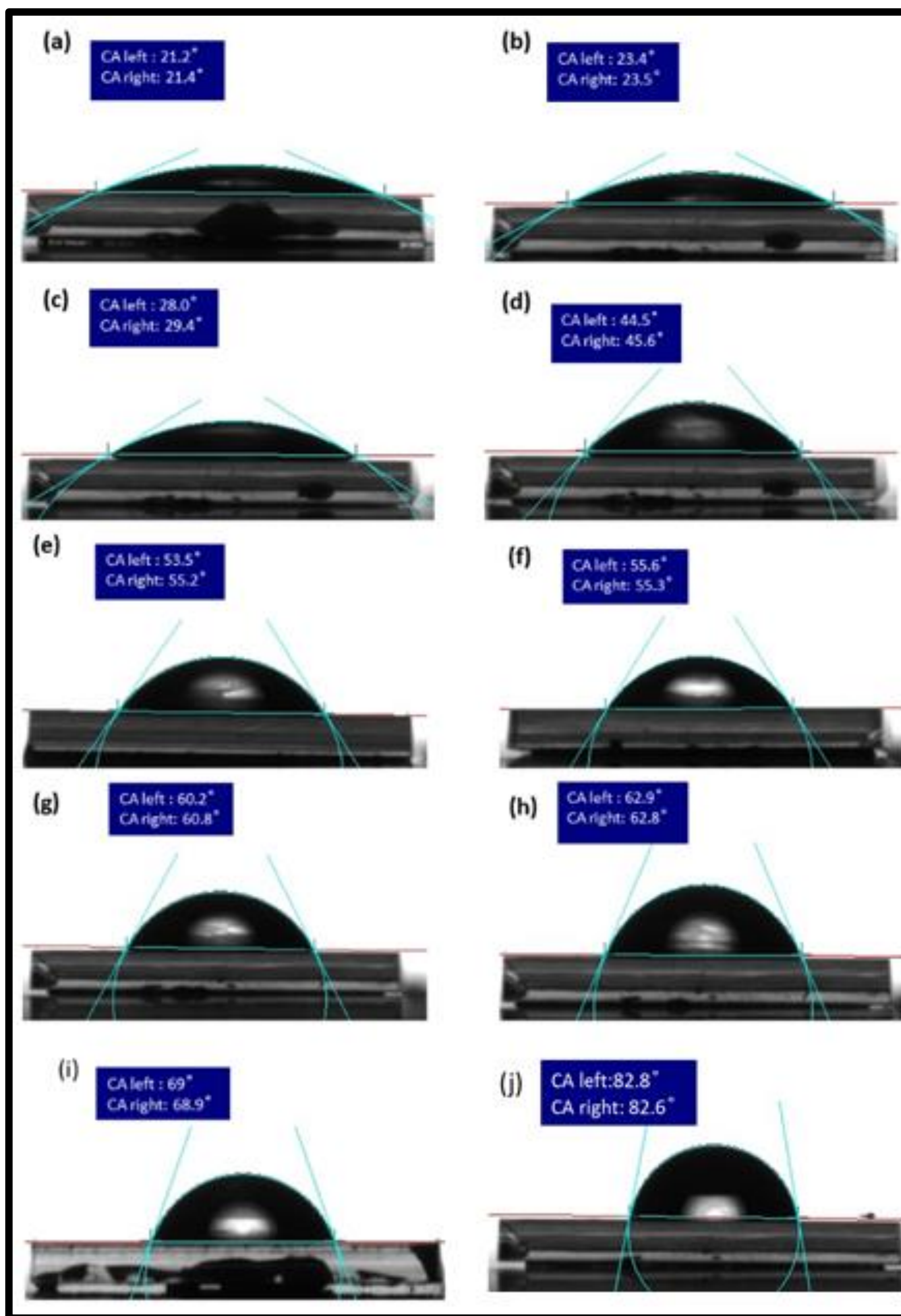

Figure 4.2.3 Droplet shape on 50 u.c. Lu2O3 film after (a)0 hr, (b)1 hr, (c)3 hr, (d)12 hr, (e)36 hr, (f)72 hr, (g)1 week, (h)2 weeks, (i)3 weeks and (j)5 weeks of exposure to ambient atmosphere.

In a different experiment, Lu_2O_3 film (~50 u.c.) and TiO_2 film (~50 nm) were prepared using PLD and immediately transferred to vacuum chamber (1xE-7 torr). The samples were stored in vacuum for 5 days and after that the WCA was recorded. WCA for these films is shown in figure 4.2.4. WCA measured immediately after storage for 5 days in vacuum is higher than the films exposed to ambient atmosphere for 5 days. There is an initial dip in WCA on exposure to ambient atmosphere and then it starts increasing on prolonged exposure to ambient atmosphere. Lu_2O_3 film WCA becomes hydrophobic (>90°) after 5 weeks of exposure to ambient following vacuum storage.

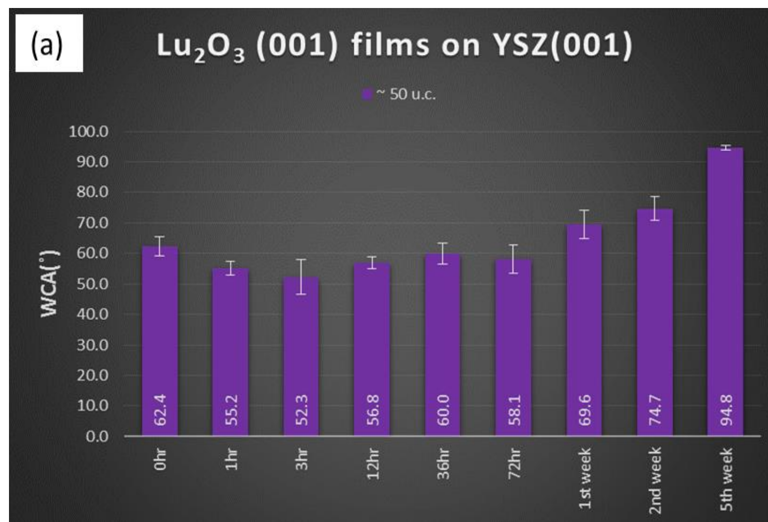

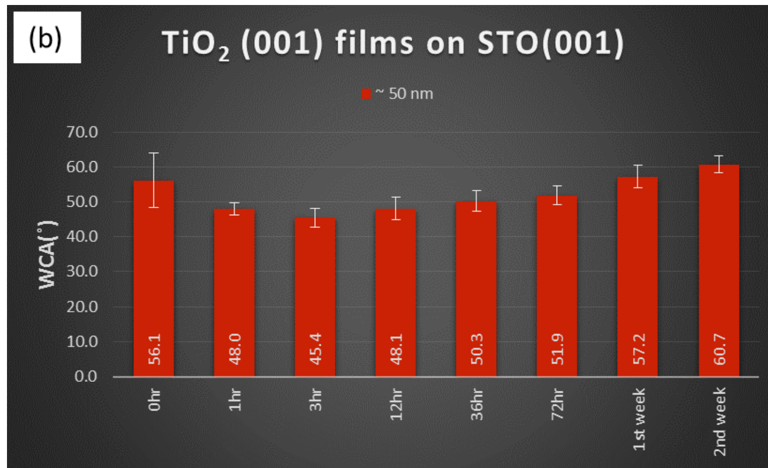

Figure 4.2.4 Average WCA for (a) Lu_2O_3 (b) TiO_2 (~50nm) film after 5days storage in vacuum(1xE-7 torr)

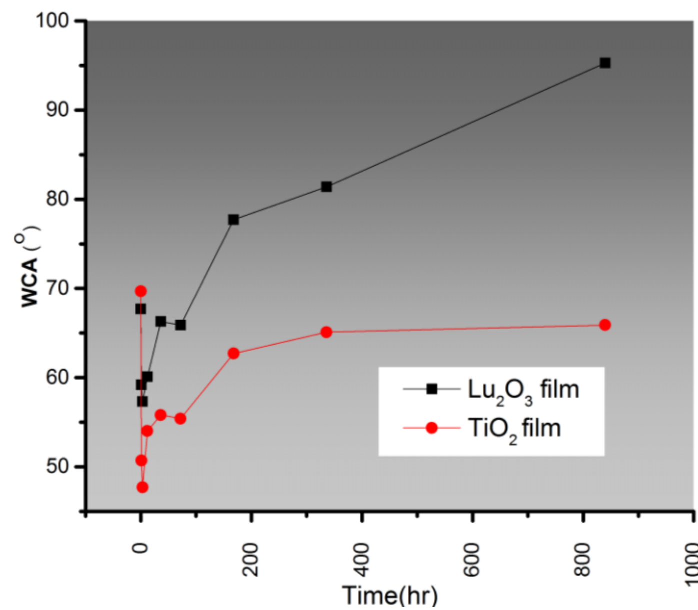

Figure 4.2.5 1st WCA for Lu_2O_3 and TiO_2 film after 5 days of storage in vacuum

The nature of temporal evolution (shown in figure 4.2.5) for both the films following storage in vacuum for 5 days is similar. The WCA for Lu_2O_3 film is still increasing after 5 weeks of exposure to ambient atmosphere while for TiO_2 appears to saturate around ~65°.

In order to understand the phenomenon that is causing the WCA of the REO films to increase with time, XPS measurements were done on three Lu_2O_3 film samples: freshly prepared, stored in ambient atmosphere for 3 weeks and stored in vacuum chamber for 5 days. The survey spectrum along with surface chemistry for these films and WCA is shown in figure 4.2.6.

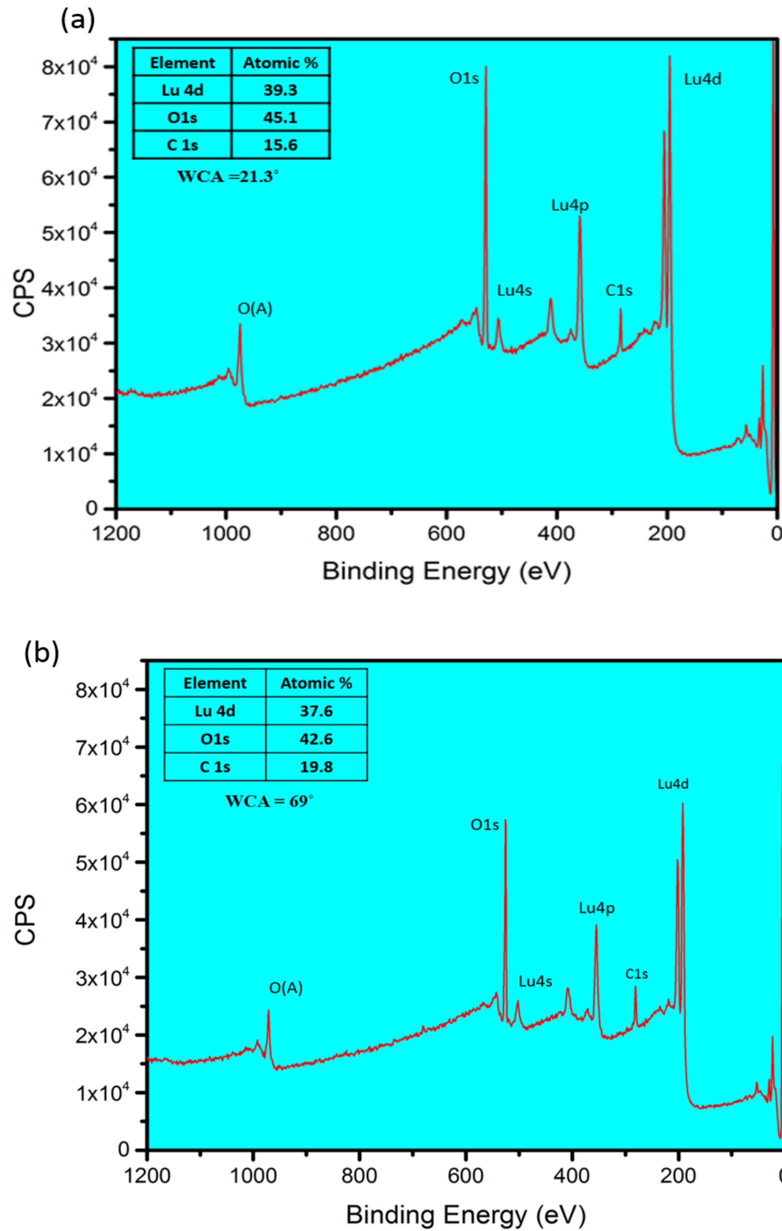

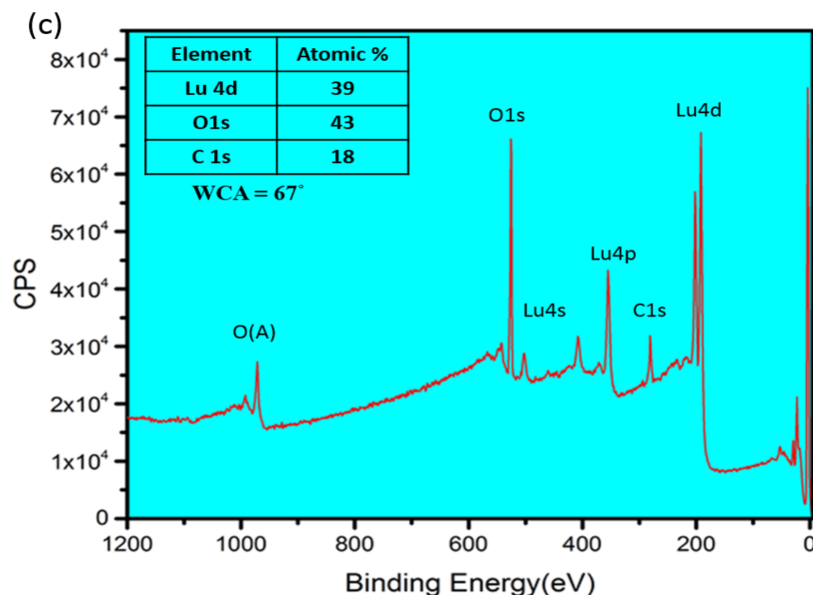

Figure 4.2.6 XPS survey spectrum of Lu_2O_3 films (a)freshly prepared(b)stored in ambient atmosphere for 3 weeks and (c)stored in vacuum for 5 days with surface composition and WCA values

The amount of hydrocarbon adsorbed on the surface is higher for the sample exposed to atmosphere and the one stored in vacuum chamber (1xE-7 torr) as compared to freshly prepared film. The high value of carbon in case of freshly prepared sample is probably due to the ex-situ nature of XPS measurement.

High resolution XPS scan C1s, O1s and Lu4d peak for the films is shown in figure 4.2.7. The C1s peak has only one peak at ~ 285 eV which corresponds to hydrocarbons with C-C and C-H bonds. The O1s peak showed one peak at ~529.6 eV corresponding to O-Lu species and a shoulder peak at ~531.7 eV which is due to the hydroxide species on the surface [54]. The Lu 4d 5/2 and Lu 4d 3/2 are separated by ~10 eV agreement with the reported literature [54-56].

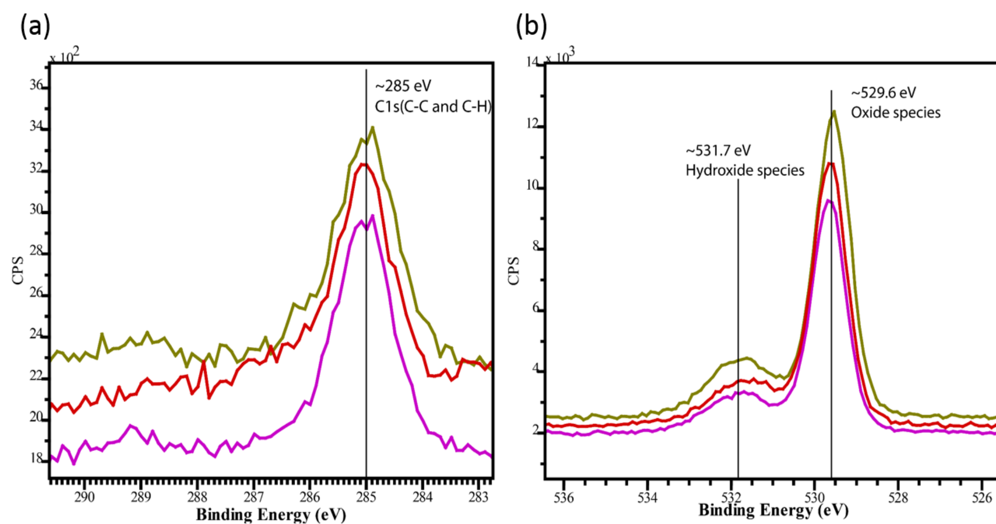

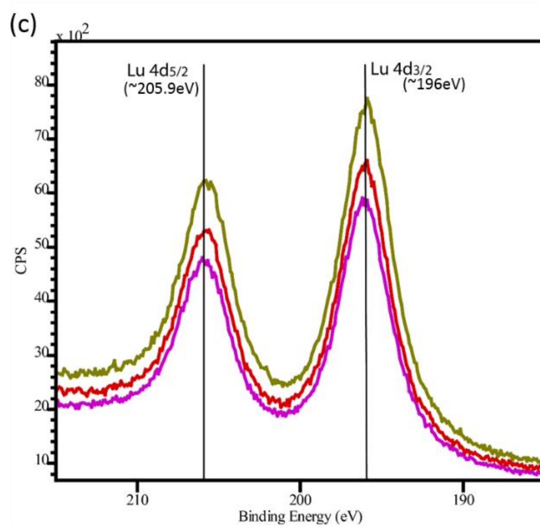

Figure 4.2.7 High resolution (a) C1s and (b) O1s and (c) Lu 4d spectra for the three Lu_2O_3 films.

4.3 CONCLUSION

All the oxides investigated in this work are intrinsically hydrophilic in nature including the REOs which were reported to be hydrophobic in some studies. We found that the existing proposed models suggesting direct interaction between the oxide chemistry and water molecule is not a factually correct representation of the situation. There is always an adsorbed layer of hydrocarbon species and water on the oxide film surface. The affinity of the surface for these adsorbed species is so strong that it cannot be prevented even by storage in vacuum of the order of 1xE-7 torr. The nature of temporal evolution of WCA suggests that a universal process is occurring on all of these oxide which lowers the surface energy and surface polarity of the films.

It is because of this process that there is such a big scatter in WCA values of similar oxide films reported in literature. Depending on the time delay between the measurement and synthesis we can get any value for WCA. However, the important question as to why the saturation value of WCA for REOs and TiO_2 is different needs further exploration for a complete explanation.

The intrinsic value of WCA for films of ~2 u.c thickness is invariably lower than the thicker films. This observation was made following measurements on many samples of each type and it was always the case.

Other important findings are as follows:

1. The environmentally saturated value of WCA for the REO films on YSZ (001) is shown in table 4.3.1.

Table 4.3.1 Environmentally saturated WCA for REO film series.

Film	Environmentally saturated WCA
CeO_2(001) on YSZ(001)	80.6±4.2°
Eu_2O_3 (001)(123) textured film on YSZ(001)	85.3±2.9°
Dy_2O_3 (001)(123) textured film on YSZ(001)	92.8±3°
Ho_2O_3 (001) on YSZ(001)	93±4.4°
Er_2O_3 (001) on YSZ(001)	89.8±3.2°
Tm_2O_3 (001) on YSZ(001)	76.9±2.8°
Yb_2O_3 (001) on YSZ(001)	79.6±3°
Lu_2O_3 (001) on YSZ(001)	84.4±2.1°

Hence, it is necessary to report the time after fabrication of the sample at which the WCA data was recorded. It is now obvious that there is undeniable process of environmental stabilization that takes place on the surface of thin films. We observe that after this stabilization, REO films approach hydrophobicity.

2. The intrinsic WCA for films in this study are shown in the table 4.3.2.

Table 4.3.2 Intrinsic WCA for oxide films.

Film	Intrinsic WCA
Lu_2O_3 (~2 u.c.)(001) on YSZ (001)	16.8±2.9 °
Lu_2O_3 (~10 u.c.)(001) on YSZ (001)	23.4±2.4 °
Lu_2O_3 (~50 u.c.)(001) on YSZ (001)	21.1± 0.7 °
Er_2O_3 (~2 u.c.)(001) on YSZ (001)	11.8±0.7 °
Er_2O_3 (~10 u.c.)(001) on YSZ (001)	15.5±0.5 °
Er_2O_3 (~50 u.c.)(001) on YSZ (001)	17.6±1.1 °
TiO_2 (~50 nm)(001) on STO(001)	9.4±1 °

3. The scatter in the reported WCA values, we now understand, is due to the difference in film roughness, different cleaning protocols involved prior to

measurement, measurement done after different time delay after synthesis/preparation, storage of samples in different conditions viz. vacuum or ambient conditions.

There is a need to develop a standard protocol for measurement of intrinsic WCA to address this. Cleaning with Acetone and DI water is not a good choice as the WCA that we get is not close to the intrinsic value or to the environmentally stable WCA which is relevant from engineering standpoint.

A good method for addressing these shortfalls and to get relevant and reproducible WCA is to use vacuum deposition techniques like PLD, Sputtering to grow a fresh homoepitaxial/ heteroepitaxial layer of the oxide film and then measuring the WCA on the pristine film immediately out of the vacuum chamber. This approach will give us the intrinsic WCA value.

Then the samples can be stored in ambient atmosphere for a period exceeding a month. The value of WCA we measure after this is the saturation value subsequent to environmental stabilization.

4. The WCA values for all the oxide films as a function of time suggests that there is a universal atmospheric stabilization phenomenon common for oxide which decreases the polarity of the surface and increases the WCA.

5. The intrinsic WCA of REO films measured immediately suggests that the films are intrinsically hydrophilic but over time due to atmospheric stabilization the WCA temporally increases to saturate at a relatively hydrophobic value.

6. The intrinsic WCA value for ~2 u.c. films of both erbium oxide and lutetium oxide are lower than their thicker films which suggests thickness dependence of intrinsic WCA. This dependence may be due to some influence from the substrate underneath or may be a direct consequence of surface energy increase due to reduction in thickness. Once the atmospheric stabilization sets in this relation is not seen. Eventually films of different thickness have roughly the same saturation value of WCA.

7. From the XPS studies done on three Lu_2O_3 samples namely freshly prepared, exposed to ambient atmosphere for 3 weeks and the one stored in vacuum for 5 days suggest that there are two processes happening on the surface which is responsible for evolution of WCA: hydration and hydrocarbon adsorption. The affinity of the freshly prepared film is so strong for water that all the three samples, one freshly prepared, one exposed to ambient and third stored in vacuum for 5 days showed the presence of around 10-12% hydroxide species on the surface. The formation of hydroxide species on the surface of other metal oxide films have been reported earlier and it is understood to cause a decrease in the WCA [57].

8. The WCA of the films after exposure to ambient is found to increase with increase in the amount of hydrocarbon adsorbed on the surface which suggests that the higher WCA on exposure to ambient atmosphere, is in part due to the layer of adsorbed hydrocarbon that builds up on the surface.

APPENDIX

A1

A1.1 Pulsed Laser Deposition (PLD)

Targets for the REOs were prepared from 99.99% pure powder supplied by Alfa Aesar. The targets were prepared by the process described in methods. The sintering temperature was in the range 1400-1600˚C depending on the melting point of individual powders.

YSZ (001) substrates was cleaned by the procedure described in methods.

Table A1. 1 PLD growth parameters for REO films.

Parameter	Value	Units
O_2 pressure	1	mtorr
Substrate temperature	800	˚C
Laser fluence	~1.8	J/cm^2
Spot size	4.5	mm^2
Repetition rate	5	Hz
No. of laser pulse	27000	shots
Base pressure	~1xE-7	torr

A1.2 Thickness of films

Thickness of the film was measured by placing a masked Si substrate adjacent to the YSZ (001) substrate for deposition. The height of the step created between the deposited and masked region was measured using profilometer. Thickness of different REO films is shown in table A1.2.

Table A1. 2 Thickness of different REO films**.**

Film	Thickness
Lu_2O_3	~210 nm
Yb_2O_3	~250 nm
Tm_2O_3	~250 nm
Er_2O_3	~230 nm
Ho_2O_3	~270 nm
Dy_2O_3	~235 nm
Eu_2O_3	~320 nm
CeO_2	~350 nm

A1.3 X-Ray Diffraction (XRD)

The 2θ/ω scans for the REO films is shown in figure A1.1. Peak position for the films correspond well with their respective cubic phases with unit cell parameters shown in table A1.3.

Table A1. 3 Crystal Structure and Lattice parameter for REOs (*Source: Crystallography Open Database*)

Film	Crystal Structure	Lattice parameter(Å)
Lu_2O_3	Cubic	10.39
Yb_2O_3	Cubic	10.43
Tm_2O_3	Cubic	10.49
Er_2O_3	Cubic	10.54
Ho_2O_3	Cubic	10.58
Dy_2O_3	Cubic	10.66
Eu_2O_3	Cubic	10.84
CeO_2	Cubic	5.41

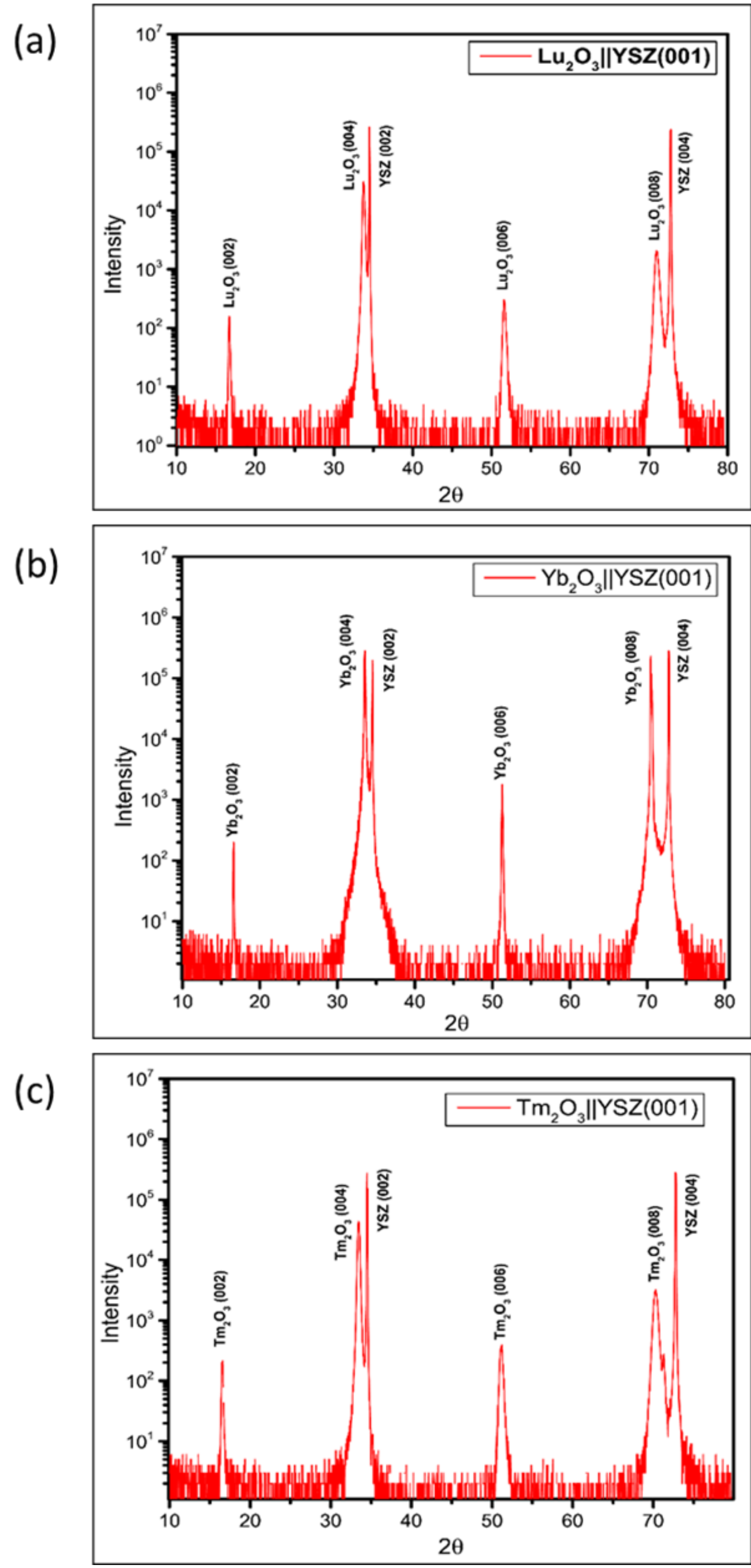
(a)
Lu2O3||YSZ(001)
Lu2O3 (002)
Lu2O3 (004)
YSZ (002)
Lu2O3 (006)
Lu2O3 (008)
YSZ (004)
Intensity
2θ
(b)
Yb2O3||YSZ(001)
Yb2O3 (002)
Yb2O3 (004)
YSZ (002)
Yb2O3 (006)
Yb2O3 (008)
YSZ (004)
Intensity
2θ
(c)
Tm2O3||YSZ(001)
Tm2O3 (002)
Tm2O3 (004)
YSZ (002)
Tm2O3 (006)
Tm2O3 (008)
YSZ (004)
Intensity
2θ

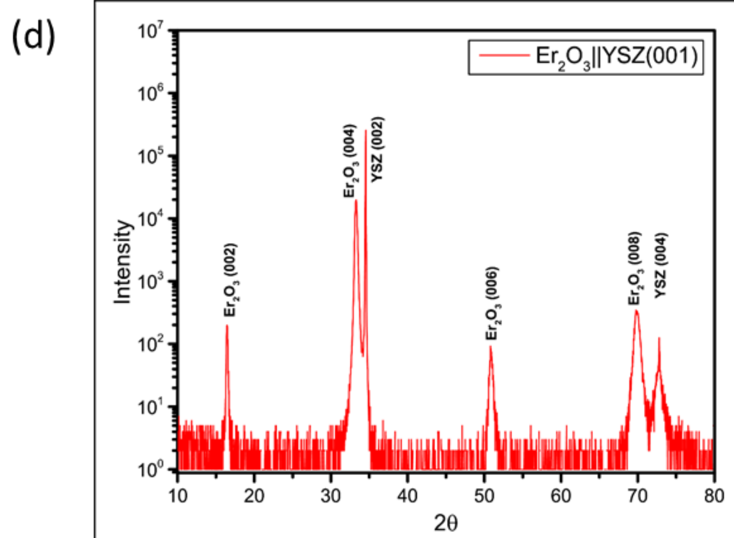
(d)
Er2O3||YSZ(001)
Intensity
2θ
Er2O3 (002)
Er2O3 (004)
YSZ (002)
Er2O3 (006)
Er2O3 (008)
YSZ (004)
10^0
10^1
10^2
10^3
10^4
10^5
10^6
10^7
10
20
30
40
50
60
70
80

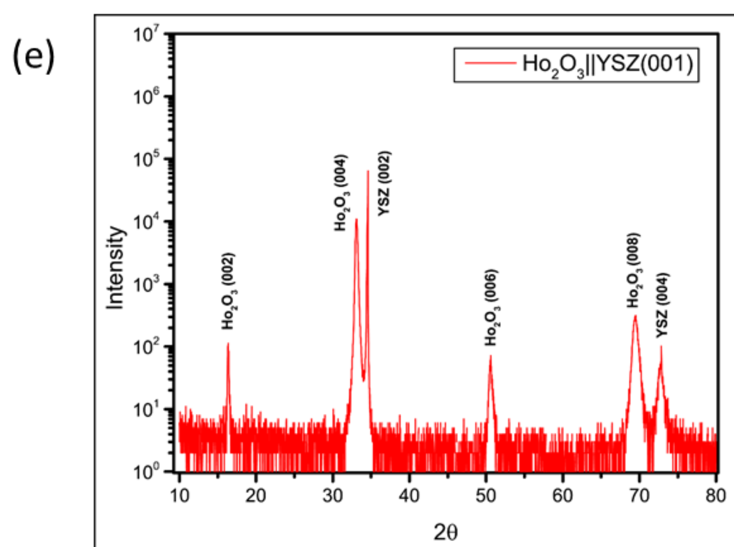
(e)
Ho2O3||YSZ(001)
Intensity
2θ
Ho2O3 (002)
Ho2O3 (004)
YSZ (002)
Ho2O3 (006)
Ho2O3 (008)
YSZ (004)
10^0
10^1
10^2
10^3
10^4
10^5
10^6
10^7
10
20
30
40
50
60
70
80

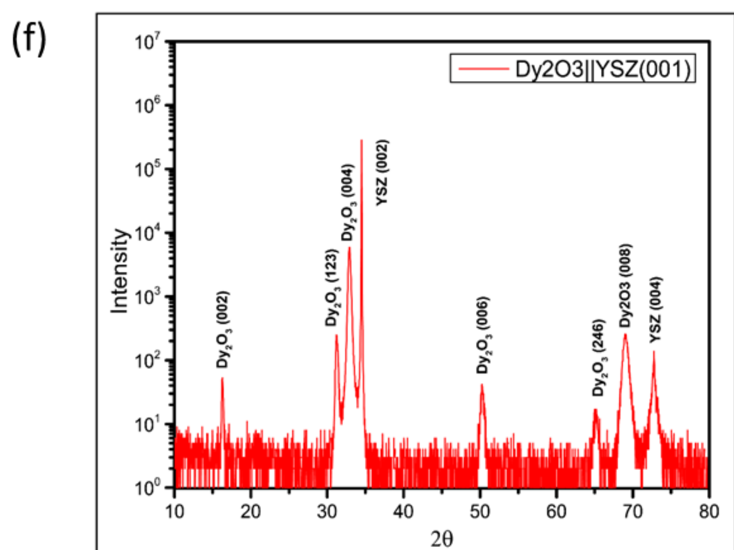
(f)
Dy2O3||YSZ(001)
Intensity
2θ
Dy2O3 (002)
Dy2O3 (123)
Dy2O3 (004)
YSZ (002)
Dy2O3 (006)
Dy2O3 (246)
Dy2O3 (008)
YSZ (004)
10^0
10^1
10^2
10^3
10^4
10^5
10^6
10^7
10
20
30
40
50
60
70
80

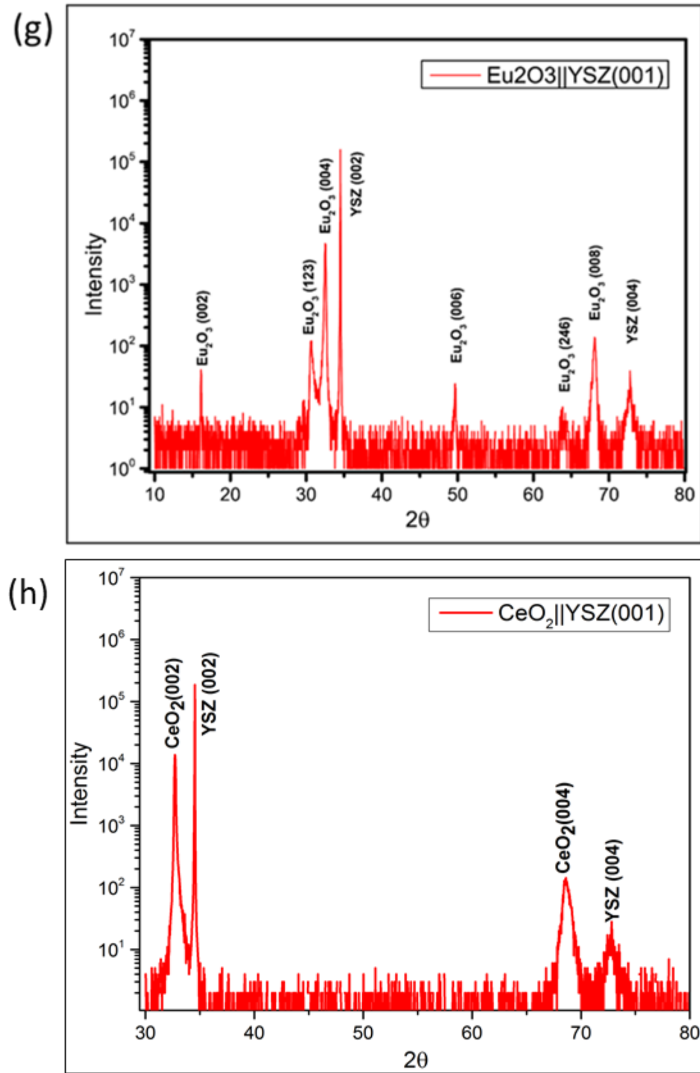

Figure A1. 1 2θ/ω scan for (a)Lu_2O_3 (b)Yb_2O_3 (c)Tm_2O_3 (d)Er_2O_3 (e)Ho_2O_3 (f)Dy_2O_3 (g)Eu_2O_3 (h)CeO_2 films on YSZ(001)

A1.4 Atomic Force Microscopy (AFM)

The AFM images for the REO thin films is shown in figure A1.2. All the films have a very low roughness to affect the WCA.

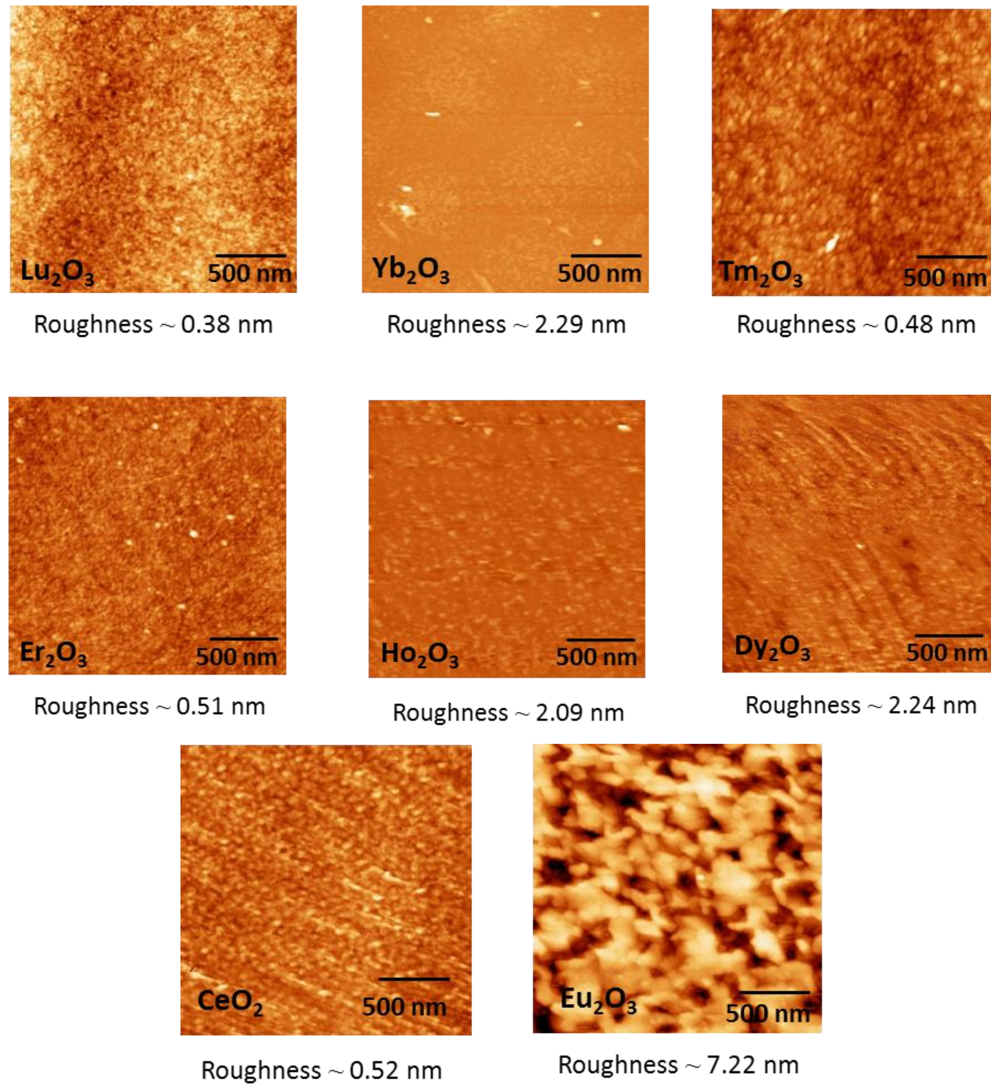

Figure A1. 2 AFM scan images for REO films with rms roughness.

A2

A2.1 Pulsed Laser Deposition (PLD)

Erbium oxide (Er_2O_3) target was prepared from 99.99% pure powder supplied by Alfa Aesar. TiO_2 target was prepared from 99.99% pure powder supplied by Sigma Aldrich. The target was sintered at 1400˚C and 1200 ˚C respectively. The YSZ (001) and STO (001) substrates were cleaned by the procedure discussed in methods.

The growth conditions for Er_2O_3 films on YSZ (001) and TiO_2 films on STO (001) shown in table A2.1 and table A2.2 respectively.

Table A2. 1 PLD growth parameters for Er_2O_3.

Parameter	Value	Units
O_2 pressure	1	mtorr
Substrate temperature	800	˚C
Laser fluence	~1.8	J/cm^2
Spot size	4.5	mm^2
Repetition rate	2	Hz
No. of laser pulse	4000	shots
Base pressure	~1xE-7	torr

Table A2. 2 PLD growth parameters for TiO_2**.**

Parameter	Value	Units
O_2 pressure	3	mtorr
Substrate temperature	700	˚C
Laser fluence	~1.7	J/cm^2
Spot size	4.5	mm^2
Repetition rate	2	Hz
No. of laser pulse	4000	shots
Base pressure	~1xE-7	torr

A2.2 Reflective High Energy Electron Diffraction (RHEED) and X-ray Reflectometry (XRR)

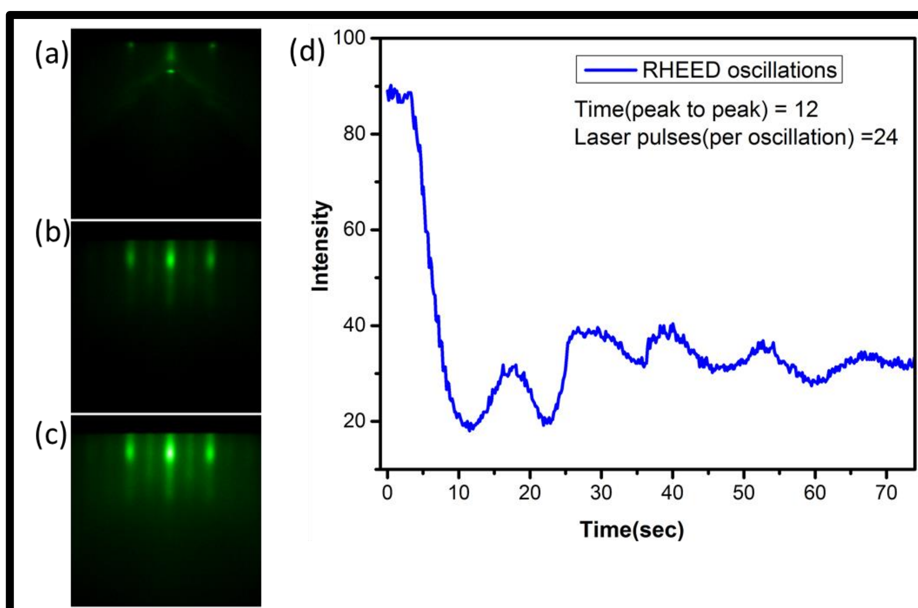

Figure A2. 1 RHEED pattern (a) YSZ substrate before deposition,(b) after 1000 laser pulses, (c) after 4000 laser pulses for erbium oxide film. (d) RHEED oscillations of the specularly reflected (00) spot during deposition.

The RHEED pattern for the film during deposition is streaky which is characteristic of epitaxial films as shown in figure A2.1 (b) and (d). A streak appears roughly midway between the (10) and ($\bar{1}$0) spot for YSZ substrate shown in figure A2.1 (a). This corresponds to the (10) and ($\bar{1}$0) of the Er_2O_3 film as the lattice parameter of Er_2O_3 is 1.054 nm which is more than twice the unit cell parameter of cubic YSZ

0.514nm. The lattice mismatch is about 2.5%.The in plane orientation relationship is $[100]_{Er2O3}$ || $[100]_{YSZ}$.

XRR was done for the Er_2O_3 film prepared. The thickness of the film was calculated by the spacing between the oscillations and also by the simulation software Leptos to be ~47 nm.

<u>Growth rate of Er_2O_3</u>

1 u.c. ≈ 1.054 nm

Growth rate ≈ 4000/47 shots/nm

≈ 85 shots/nm

≈ 90 shots/ u.c.

About 4 intensity oscillations were observed in the specular (00) reflection for ~96 laser pulses as shown in figure A2.1 (d). Hence, it takes about 4 RHEED oscillations (~96 shots) for deposition of 1 u.c. thick Er_2O_3 film on YSZ (001) with the deposition parameters used.

A2.3 X-ray Diffraction (XRD)

The XRD scans for the Er_2O_3 film are shown in figure A2.2.The structure of bulk lutetium oxide is cubic with a lattice parameter of 10.54 Å. The 2θ position for the peaks corresponds well with the (0 0 *l*) lattice planes of the film and substrate. The out-of-plane orientation relationship between the film and substrate is hence $(001)_{Er2O3}$ || $(001)_{YSZ}$. The d-spacing for the (001) plane of lutetium oxide film is

elongated ~10.67 Å. The effective structure of lutetium oxide in the film due to epitaxial strain becomes tetragonal.

The rocking curve (figure A2.2 (b)) for (004) peak of the film is ~0.14° indicating good crystallinity of the film. XRD analysis shows that the film is single crystal with out-of-plane epitaxial relationship $(001)_{Er2O3}$ || $(001)_{YSZ}$.

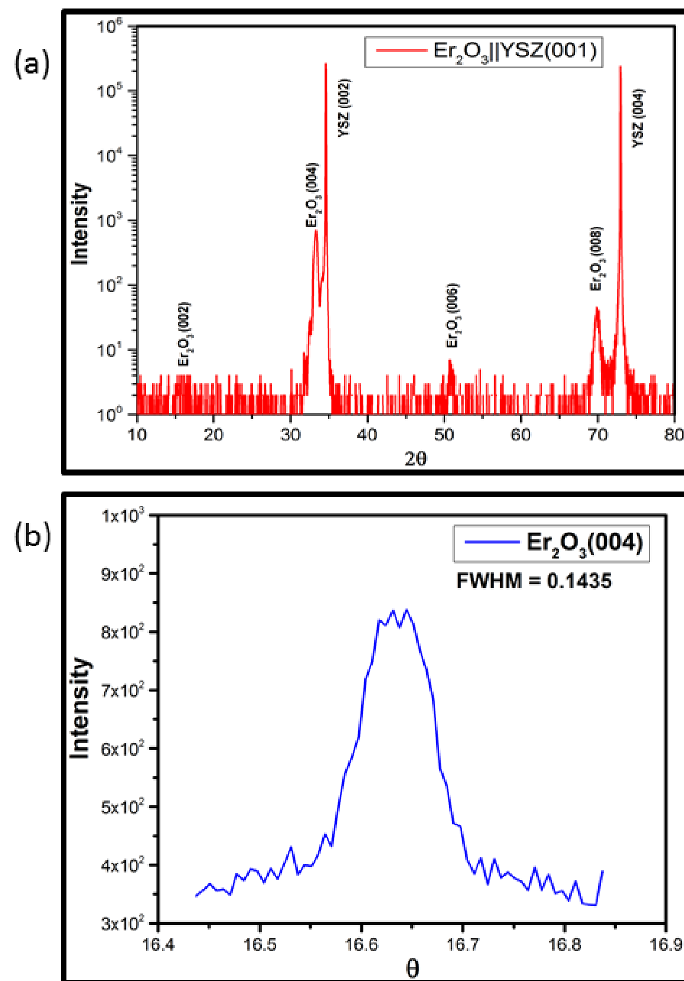

Figure A2. 2 (a) 2θ/ω plot (b) rocking curve about (004) of Er_2O_3 film

Figure A2.3 shows the XRD scan results for TiO_2 film. The 2θ position of peak corresponds well with (004) reflection of the tetragonal Anatase phase of TiO_2. Φ scan for {015} family for the film shows only four equally spaced peaks (separation

90˚) which is consistent with the 4-fold symmetry of the tetragonal structure of anatase titanium dioxide film. The film is single crystal with out-of-plane epitaxial relationship $(001)_{TiO2} \| (001)_{STO}$.

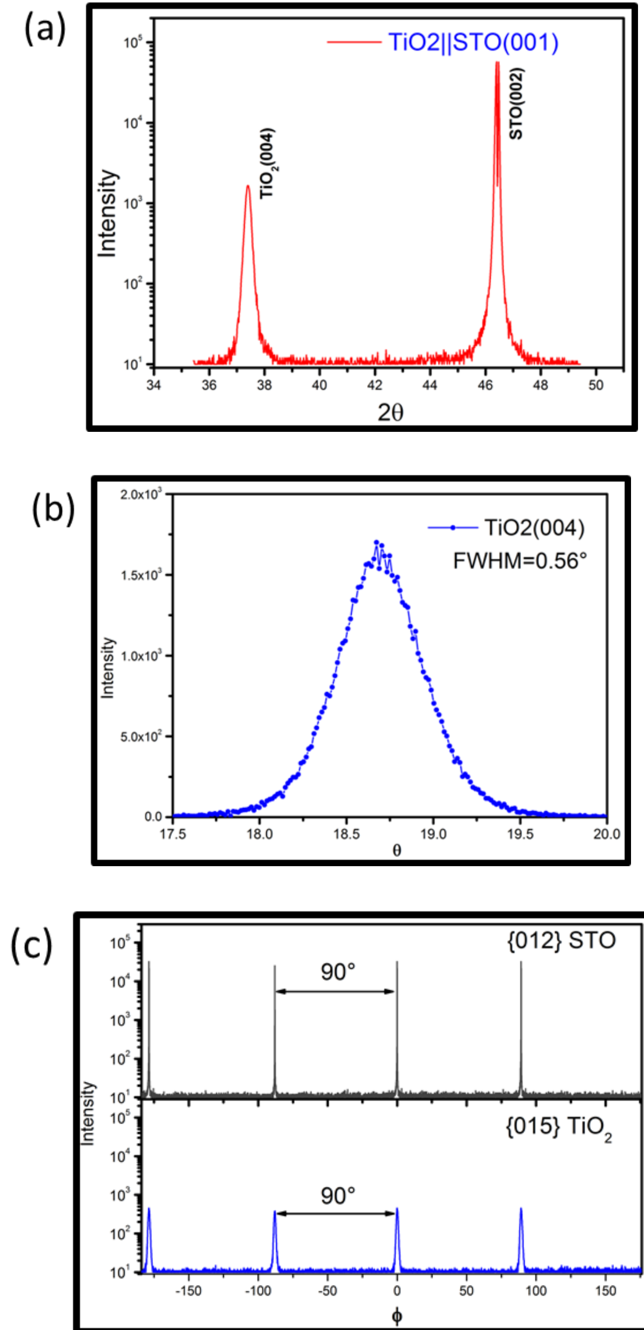

Figure A2. 3 (a) 2θ/ω plot of titanium dioxide film on STO (001) (b) rocking curve about (004) peak of TiO_2 (c) phi scan TiO_2 {015}.

A2.4 Atomic Force Microscope

The AFM scan images for the Er_2O_3 and TiO_2 film is shown in figure A2.4. The films are very smooth.

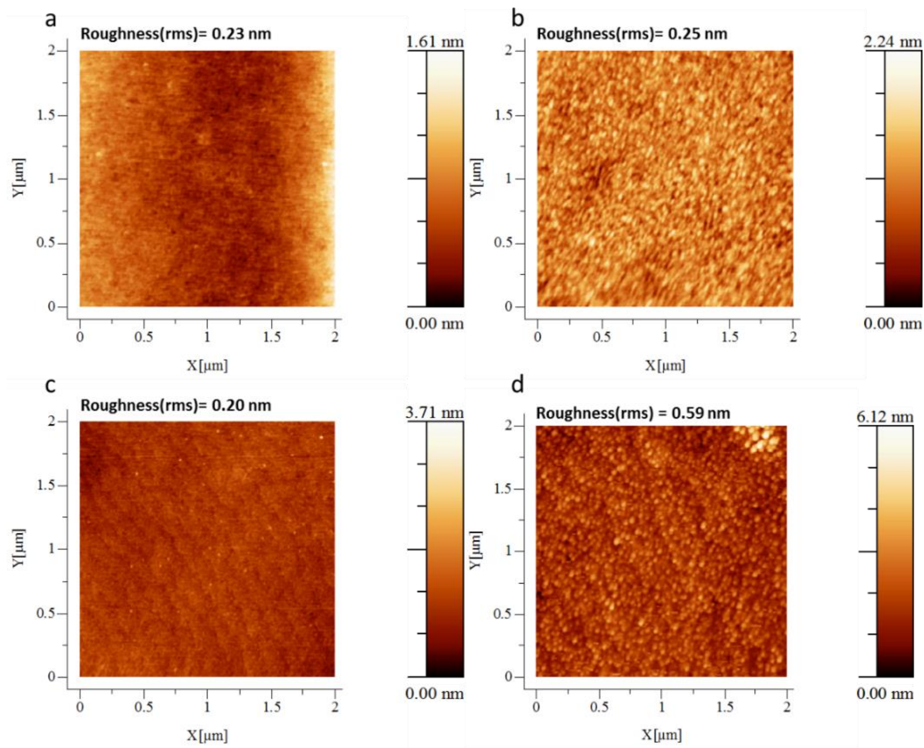

Figure A2. 4 AFM images with rms roughness values for (a) YSZ (001) substrate, (b) Er_2O_3 film, (c) STO (001) substrate and (d) TiO_2 film.

REFERENCES

1. de Gennes, P.G., *Wetting: statics and dynamics.* Reviews of Modern Physics, 1985. **57**(3): p. 827-863.
2. Yao, L. and J. He, *Recent progress in antireflection and self-cleaning technology – From surface engineering to functional surfaces.* Progress in Materials Science, 2014. **61**: p. 94-143.
3. Blossey, R., *Self-cleaning surfaces [mdash] virtual realities.* Nat Mater, 2003. **2**(5): p. 301-306.
4. Yang, H. and P. Jiang, *Self-Cleaning Diffractive Macroporous Films by Doctor Blade Coating.* Langmuir, 2010. **26**(15): p. 12598-12604.
5. Bhushan, B., Y.C. Jung, and K. Koch, *Self-Cleaning Efficiency of Artificial Superhydrophobic Surfaces.* Langmuir, 2009. **25**(5): p. 3240-3248.
6. Yuan, Y. and T.R. Lee, *Contact angle and wetting properties*, in *Surface science techniques*. 2013, Springer. p. 3-34.
7. Chadwell, H.M., *The Molecular Structure of Water.* Chemical Reviews, 1928. **4**(4): p. 375-398.
8. Young, T., Philos. Trans. R. Soc. London, 1805. **95**: p. 65.
9. Marmur, A., *Solid-Surface Characterization by Wetting*, in *Annual Review of Materials Research*. 2009, Annual Reviews: Palo Alto. p. 473-489.
10. Yoon, R.H., D.H. Flinn, and Y.I. Rabinovich, *Hydrophobic Interactions between Dissimilar Surfaces.* J Colloid Interface Sci, 1997. **185**(2): p. 363-70.
11. Berg, J.M., et al., *Three-Component Langmuir-Blodgett Films with a Controllable Degree of Polarity.* Langmuir, 1994. **10**(4): p. 1225-1234.
12. Liu, K. and L. Jiang, *Metallic surfaces with special wettability.* Nanoscale, 2011. **3**(3): p. 825-838.
13. Wenzel, R.N., *Surface Roughness and Contact Angle.* The Journal of Physical and Colloid Chemistry, 1949. **53**(9): p. 1466-1467.
14. Cassie, A.B.D., Disc. Faraday Soc., 1948. **3**: p. 11.
15. Nakajima, A., K. Hashimoto, and T. Watanabe, *Recent studies on super-hydrophobic films.* Monatshefte für Chemie/Chemical Monthly, 2001. **132**(1): p. 31-41.
16. Sakai, N., et al., *Quantitative Evaluation of the Photoinduced Hydrophilic Conversion Properties of TiO2 Thin Film Surfaces by the Reciprocal of Contact Angle.* The Journal of Physical Chemistry B, 2003. **107**(4): p. 1028-1035.
17. Sun, R.-D., et al., *Photoinduced Surface Wettability Conversion of ZnO and TiO2 Thin Films.* The Journal of Physical Chemistry B, 2001. **105**(10): p. 1984-1990.
18. Wang, R., et al., *Photogeneration of Highly Amphiphilic TiO2 Surfaces.* Advanced Materials, 1998. **10**(2): p. 135-138.
19. Sakai, N., et al., *Effect of Ultrasonic Treatment on Highly Hydrophilic TiO2 Surfaces.* Langmuir, 1998. **14**(20): p. 5918-5920.
20. Miyauchi, M., et al., *Photoinduced Surface Reactions on TiO2 and SrTiO3 Films: Photocatalytic Oxidation and Photoinduced Hydrophilicity.* Chemistry of Materials, 2000. **12**(1): p. 3-5.
21. Azimi, G., et al., *Hydrophobicity of rare-earth oxide ceramics.* Nat Mater, 2013. **12**(4): p. 315-20.

22. Adachi, G., N. Imanaka, and Z.C. Kang, *Binary Rare Earth Oxides*. 2004.
23. Topp, N.E., *The Chemistry of The Rare Earth Elements*. 1965.
24. Giovambattista, N., P.G. Debenedetti, and P.J. Rossky, *Effect of surface polarity on water contact angle and interfacial hydration structure.* J. Phys. Chem. B, 2007. **111**: p. 9581-9587.
25. Stirnemann, G., et al., *Water reorientation, hydrogen-bond dynamics and 2D-IR spectroscopy next to an extended hydrophobic surface.* Faraday Discuss., 2010. **146**: p. 263-281.
26. Drzymala, J., *Hydrophobicity and collectorless flotation of inorganic materials.* Adv. Colloid Interface Sci., 1994. **50**: p. 143-185.
27. Du, Q., E. Freysz, and R. Shen, *Surface vibrational spectroscopic studies of hydrogen bonding and hydrophobicity.* Science, 1994. **264**: p. 826-828.
28. Scatena, L.F., M.G. Brown, and G.L. Richmond, *Water at hydrophobic surfaces: Weak hydrogen bonding and strong orientation effects.* Science, 2001. **292**: p. 908-912.
29. Zenkin, S., et al., *Hydrophobicity of Thin Films of Compounds of Low-Electronegativity Metals.* Journal of the American Ceramic Society, 2014. **97**(9): p. 2713-2717.
30. Preston, D.J., et al., *Effect of hydrocarbon adsorption on the wettability of rare earth oxide ceramics.* Applied Physics Letters, 2014. **105**(1): p. 011601.
31. Erb, R.A., *Wettability of Metals under Continuous Condensing Conditions.* The Journal of Physical Chemistry, 1965. **69**(4): p. 1306-1309.
32. Bewig, K.W. and W.A. Zisman, *The Wetting of Gold and Platinum by Water.* The Journal of Physical Chemistry, 1965. **69**(12): p. 4238-4242.
33. Khan, S., et al., *Role of surface oxygen-to-metal ratio on the wettability of rare-earth oxides.* Applied Physics Letters, 2015. **106**(6): p. 061601.
34. Kwon, H.-M., *Tailoring hydrodynamics of non-wetting droplets with nano-engineered surfaces*. 2013, Massachusetts Institute of Technology.
35. Azimi, G., H.-M. Kwon, and K.K. Varanasi, *Superhydrophobic surfaces by laser ablation of rare-earth oxide ceramics.* MRS Communications, 2014: p. 1-5.
36. Oh, I.-K., et al., *Hydrophobicity of Rare Earth Oxides Grown by Atomic Layer Deposition.* Chemistry of Materials, 2015. **27**(1): p. 148-156.
37. Smith, H.M. and A.F. Turner, *VACUUM DEPOSITED THIN FILMS USING A RUBY LASER.* Applied Optics, 1965. **4**(1): p. 147-&.
38. Dijkkamp, D., et al., *Preparation of Y-Ba-Cu oxide superconductor thin films using pulsed laser evaporation from high Tc bulk material.* Applied Physics Letters, 1987. **51**(8): p. 619.
39. Jackson, T.J. and S.B. Palmer, *OXIDE SUPERCONDUCTOR AND MAGNETIC METAL THIN-FILM DEPOSITION BY PULSED-LASER ABLATION - A REVIEW.* Journal of Physics D-Applied Physics, 1994. **27**(8): p. 1581-1594.
40. Krebs, H.-U., *Pulsed Laser Deposition of Metals*, in *Pulsed Laser Deposition of Thin Films*. 2006, John Wiley & Sons, Inc. p. 363-382.
41. Chen, C. and J.S. Horwitz, *Ferroelectric Thin Films for Microwave Device Applications*, in *Pulsed Laser Deposition of Thin Films*. 2006, John Wiley & Sons, Inc. p. 533-561.
42. Craciun, F. and M. Dinescu, *Piezoelectrics*, in *Pulsed Laser Deposition of Thin Films*. 2006, John Wiley & Sons, Inc. p. 487-532.

43. Chrisey, D.B., et al., *Laser Deposition of Polymer and Biomaterial Films.* Chemical Reviews, 2003. **103**(2): p. 553-576.
44. Krebs, H.-U., et al., *Pulsed Laser Deposition (PLD) -- A Versatile Thin Film Technique*, in *Advances in Solid State Physics*, B. Kramer, Editor. 2003, Springer Berlin Heidelberg. p. 505-518.
45. Singh, R.K. and J. Narayan, *Pulsed-laser evaporation technique for deposition of thin films: Physics and theoretical model.* Physical Review B, 1990. **41**(13): p. 8843-8859.
46. Rijnders, G. and D.H.A. Blank, *In Situ Diagnostics by High-Pressure RHEED During PLD*, in *Pulsed Laser Deposition of Thin Films*. 2006, John Wiley & Sons, Inc. p. 85-97.
47. Rijnders, G. and D.H.A. Blank, *Growth Kinetics During Pulsed Laser Deposition*, in *Pulsed Laser Deposition of Thin Films*. 2006, John Wiley & Sons, Inc. p. 177-190.
48. Rijnders, G.J.H.M., et al., *In situ monitoring during pulsed laser deposition of complex oxides using reflection high energy electron diffraction under high oxygen pressure.* Applied Physics Letters, 1997. **70**(14): p. 1888-1890.
49. Blank, D.H.A., et al., *In-situ monitoring by reflective high energy electron diffraction during pulsed laser deposition.* Applied Surface Science, 1999. **138–139**(0): p. 17-23.
50. Borisov, S.V. and N.V. Podberezskaya, *X-ray diffraction analysis: A brief history and achievements of the first century.* Journal of Structural Chemistry, 2012. **53**(1): p. 1-3.
51. Binnig, G., C.F. Quate, and C. Gerber, *Atomic Force Microscope.* Physical Review Letters, 1986. **56**(9): p. 930-933.
52. Martin, Y., C.C. Williams, and H.K. Wickramasinghe, *Atomic force microscope–force mapping and profiling on a sub 100-Å scale.* Journal of Applied Physics, 1987. **61**(10): p. 4723-4729.
53. Zhong, Q., et al., *Fractured polymer/silica fiber surface studied by tapping mode atomic force microscopy.* Surface Science Letters, 1993. **290**(1–2): p. L688-L692.
54. Padalia, B.D., et al., *The reactions of oxygen and water with the rare-earth metals terbium to lutetium studied by x-ray photoelectron spectroscopy.* Surface Science, 1976. **61**(2): p. 468-482.
55. Espinós, J.P., A.R. González-Elipe, and J.A. Odriozola, *XPS study of lutetium oxide samples with different hydration/carbonation degrees as a function of the preparation method.* Applied Surface Science, 1987. **29**(1): p. 40-48.
56. Lang, W.C., et al., *Multiplet structure in X-ray photoelectron spectra of rare earth elements and their surface oxides.* Faraday Discussions of the Chemical Society, 1975. **60**(0): p. 37-43.
57. Bayati, M.R., et al., *Ultrafast switching in wetting properties of TiO2/YSZ/Si(001) epitaxial heterostructures induced by laser irradiation.* Journal of Applied Physics, 2013. **113**(6): p. 063706.